

VIS³COS: III. environmental effects on the star formation histories of galaxies at $z \sim 0.8$ seen in [OII], H δ , and D_n4000 *

Ana Paulino-Afonso^{1,2,3,**}, David Sobral³, Behnam Darvish⁴, Bruno Ribeiro⁵, Ian Smail⁶, Philip Best⁷, Andra Stroe⁸, and Joseph Cairns³

¹ Instituto de Astrofísica e Ciências do Espaço, Universidade de Lisboa, OAL, Tapada da Ajuda, PT1349-018 Lisboa, Portugal

² Departamento de Física, Faculdade de Ciências, Universidade de Lisboa, Edifício C8, Campo Grande, PT1749-016 Lisboa, Portugal

³ Department of Physics, Lancaster University, Lancaster, LA1 4YB, UK

⁴ Cahill Center for Astrophysics, California Institute of Technology, 1216 East California Boulevard, Pasadena, CA 91125, USA

⁵ Leiden Observatory, Leiden University, P.O. Box 9513, NL-2300 RA Leiden, The Netherlands

⁶ Centre for Extragalactic Astrophysics, Department of Physics, Durham University, Durham DH1 3LE, UK

⁷ Institute for Astronomy, University of Edinburgh, Royal Observatory, Blackford Hill, Edinburgh EH9 3HJ, UK

⁸ Harvard-Smithsonian Center for Astrophysics, 60 Garden Street, Cambridge, MA 02138, USA

ABSTRACT

We present spectroscopic observations of 466 galaxies in and around a superstructure at $z \sim 0.84$ targeted by the VIMOS Spectroscopic Survey of a Supercluster in the COSMOS field (VIS³COS). We use [OII] λ 3727, H δ , and D_n4000 to trace the recent, mid-, and long-term star formation histories and investigate how stellar mass and the local environment impacts those. By studying trends both in individual and composite galaxy spectra, we find that both stellar mass and environment play a role in the observed galactic properties. Low stellar mass galaxies ($10 < \log_{10}(M_\star/M_\odot) < 10.5$) in the field show the strongest H δ absorption. Similarly, the massive population ($\log_{10}(M_\star/M_\odot) > 11$) shows an increase in H δ absorption strengths in intermediate-density environments (e.g. filaments). Intermediate stellar mass galaxies ($10.5 < \log_{10}(M_\star/M_\odot) < 11$) have similar H δ absorption profiles in all environments, but show a hint of enhanced [OII] emission at intermediate-density environments. This hints that low stellar mass field galaxies and high stellar mass filament galaxies are more likely to have experienced a recent burst of star formation, while galaxies of the intermediate stellar-mass show an increase of star formation at filament-like densities. We also find that the median [OII] equivalent width ($|EW_{[OII]}|$) decreases from $27 \pm 2 \text{ \AA}$ to $2.0^{+0.5}_{-0.4} \text{ \AA}$ and D_n4000 increases from 1.09 ± 0.01 to 1.56 ± 0.03 with increasing stellar mass (from $\sim 10^{9.25}$ to $\sim 10^{11.35} M_\odot$). Concerning the dependence on the environment, we find that at fixed stellar mass $|EW_{[OII]}|$ is tentatively lower in higher density environments. Regarding D_n4000 , we find that the increase with stellar mass is sharper in denser environments, hinting that such environments may accelerate galaxy evolution. Moreover, we find larger D_n4000 values in denser environments at fixed stellar mass, suggesting that galaxies are on average older and/or more metal-rich in such dense environments. This set of tracers depicts a scenario where the most massive galaxies have, on average, the lowest sSFRs and the oldest stellar populations (age ≥ 1 Gyr, showing a mass-downsizing effect). We also hypothesize that the observed increase in star formation (higher $|EW_{[OII]}|$, higher sSFR) at intermediate densities may lead to quenching since we find the quenched fraction to increase sharply from the filament to cluster-like regions at similar stellar masses.

Key words. galaxies: evolution – galaxies: high redshift – galaxies: star formation – large-scale structure of Universe

1. Introduction

One of the key tracers of galactic evolution is the rate at which gas is converted into stars, measured as the star formation rate (SFR, e.g. Kennicutt 1998; Kennicutt & Evans 2012). Observations show that typical galaxies were actively forming stars at a rate of ~ 10 times higher at $z \sim 2$ than at $z \sim 0$ (both the cosmic star formation rate density and typical SFRs decrease during this epoch, see e.g. Madau & Dickinson 2014; Sobral et al. 2014). One of the fundamental questions of modern Astronomy is to understand the mechanisms responsible for the regulation of star formation in galaxies and find how efficient galaxies are in con-

verting gas into stars (see e.g. Combes et al. 2013; Lehnert et al. 2013).

There are two broad groups of processes, internal and external, that can contribute to the evolution of any given galaxy (e.g. Kormendy 2013). However, the contribution of each set of processes to regulating star formation in galaxies is still unclear (see e.g. Erfanianfar et al. 2016). Internal processes include dynamical instabilities (e.g. Kormendy 2013), halo quenching (e.g. Birnboim & Dekel 2003; Kereš et al. 2005, 2009b; Dekel & Cox 2006), supernova feedback (e.g. Efstathiou 2000; Cox et al. 2006), and active galactic nuclei (AGN) feedback (e.g. Bower et al. 2006; Croton et al. 2006; Somerville et al. 2008; Fabian 2012). External processes include galaxy interactions with other galaxies or the inter galactic medium, specifically ram pressure stripping (e.g. Gunn & Gott 1972), galaxy strangulation (e.g. Larson et al. 1980; Balogh et al. 2000), galaxy-galaxy interac-

* Based on observations obtained with VIMOS on the ESO/VLT under the programmes 086.A-0895, 088.A-0550, and 090.A-0401.

** E-mail: aafonso@oal.ul.pt

tions and harassment (e.g. Mihos & Hernquist 1996; Moore et al. 1998), or tidal interaction between the large-scale gravitational potential and the galaxy (e.g. Merritt 1984; Fujita 1998). These range of physical processes are thought of being the way through which galaxies regulate, and eventually halt the formation of new stars, a phenomenon commonly referred to as galaxy quenching (e.g. Gabor et al. 2010; Peng et al. 2010b).

How each proposed mechanism affects individual galaxies is complex. In internal processes, feedback can either heat or eject the gas from galaxies preventing it from condensing in molecular clouds to form new stars (e.g. Kereš et al. 2009a). Supernova feedback is thought to be more important at lower stellar masses, and AGN feedback is arguably an important mechanism for quenching at high stellar masses (e.g. Puchwein & Springel 2013). Halo quenching refers to gravitational heating, preventing gas from cooling down and forming new stars. However, it requires a sustained mechanism to heat the gas (e.g. Birnboim et al. 2007), and cold gas flows might still penetrate the halo into the galactic disk to fuel star formation (e.g. Kereš et al. 2009b).

In terms of external processes, ram pressure stripping can initially compress the gas/dust thus increasing the column density of the gas and dust which is favourable for star formation (e.g. Gallazzi et al. 2009a; Bekki 2009; Owers et al. 2012; Roediger et al. 2014). Tidal galaxy-galaxy interactions can lead to the compression and inflow of the gas in the periphery of galaxies into the central parts, feeding and rejuvenating the stellar populations in the central galactic regions which result in an enhancement in star formation activity (e.g. Mihos & Hernquist 1996; Kewley et al. 2006; Ellison et al. 2008). Such encounters are probable when the galaxies have low relative velocities (i.e., low-velocity-dispersion environments) and are closer to each other (denser regions). Intermediate-density environments such as galaxy groups, in-falling regions of clusters, cluster outskirts, merging clusters, and galaxy filaments provide the ideal conditions for such interactions (e.g. Moss 2006; Perez et al. 2009; Li et al. 2009; Sobral et al. 2011; Tonnesen & Cen 2012; Darvish et al. 2014; Stroe et al. 2014, 2015; Malavasi et al. 2017). This enhancement of star formation is thought to be responsible for the subsequent quenching since most of the available gas is consumed or expelled through outflows in a short period of time effectively preventing future star formation from occurring in the galaxy without further external influence. If those events are ubiquitous, one should observe a temporary rise in star formation in such environments, after which galaxies are expected to become passive. This has been found in several studies, referring to the intermediate-density environments as sites of enhanced star formation rate and obscured star formation activity (e.g. Smail et al. 1999; Best 2004; Koyama et al. 2008, 2010, 2013; Gallazzi et al. 2009a; Geach et al. 2009; Sobral et al. 2011, 2016; Coppin et al. 2012; Stroe et al. 2015, 2017).

Since many of these mechanisms are linked to the increased density of galaxies, it is natural to look in over-dense regions for the impact of the local environment on the observed properties of galaxy populations. In the local Universe ($z \sim 0$), star formation is typically lower in higher density environments (e.g. Oemler 1974; Dressler 1980; Lewis et al. 2002; Kauffmann et al. 2004; Blanton et al. 2005; Li et al. 2006; Peng et al. 2010b; Darvish et al. 2016, 2018). By separating galaxies into distinct populations (star-forming and quiescent) studies find that the quenched fraction is highly dependent on the local density, at least up to $z \lesssim 1$, with the quenched population being more common in high-density regions and a higher fraction of star-forming galaxies found in lower density regions (e.g. Kodama et al. 2001, 2004; Best 2004; Nantais et al. 2013; Darvish et al. 2016; Erfanianfar

et al. 2016; Cohen et al. 2017). While in the local Universe the picture is clear, with the average star formation being the lowest in high-density, relaxed cluster regions (e.g. Balogh et al. 2000; Kauffmann et al. 2004), it is still unclear if that holds at higher redshifts. Some studies find a flattening and/or reversal of such relation ($z \sim 1 - 1.5$, e.g. Cucciati et al. 2006; Elbaz et al. 2007; Ideue et al. 2009; Tran et al. 2010; Popesso et al. 2011; Li et al. 2011; Santos et al. 2014; Stach et al. 2017; Cooke et al. 2019), while others find the same trends we see locally (e.g. Patel et al. 2009; Sobral et al. 2011; Muzzin et al. 2012; Santos et al. 2013; Scoville et al. 2013; Darvish et al. 2016). It is possible that reconciling the different observed trends requires more detailed analysis on other possible underlying relations, especially with stellar mass (e.g. Peng et al. 2010b; Sobral et al. 2011; Muzzin et al. 2012; Darvish et al. 2016), and also controlling for other properties such as AGN fraction and dust content. An alternative explanation might be the stochastic nature of the formation of dense environments which can explain the observed differences as a natural cosmic variance.

Recent studies in the literature are using spectral indices [OII], $H\delta$, and D_n4000 to probe the stellar population of galaxies at intermediate redshifts ($0.5 \lesssim z \lesssim 1.2$) due to their availability in the observed optical frame. All these indicators, when combined, can be used to distinguish actively star-forming, (post-)starburst, and old/passive galaxies since they should occupy different regions of the possible parameter space (e.g. Couch & Sharples 1987; Balogh et al. 1999; Poggianti et al. 1999, 2009; Fritz et al. 2014). The [OII] $\lambda 3737$ emission traces on-going star formation (timescales of ~ 10 Myr, e.g. Couch & Sharples 1987; Poggianti et al. 1999; Kennicutt 1998; Kewley et al. 2004; Poggianti et al. 2006), however, it depends also on the metallicity and can be a poor tracer for dusty galaxies (e.g. Kewley et al. 2004; Yan et al. 2006; Kocevski et al. 2011). By measuring the [OII] equivalent width we can also crudely trace the specific SFR (sSFR) which is found to anti-correlate with stellar mass (e.g. Bridge et al. 2015; Cava et al. 2015; Darvish et al. 2015a) with more massive star-forming galaxies having lower [OII] equivalent widths. Additionally, higher density environments are found to depress [OII] emission (e.g. Balogh et al. 1999; Darvish et al. 2015a). The $H\delta$ line (and other strong Balmer absorption lines) can be indicative of a post-starburst phase ($\approx 100 - 1000$ Myr after the burst, e.g. Couch & Sharples 1987; Balogh et al. 1999; Poggianti et al. 1999, 2009; Dressler et al. 2004; Vergani et al. 2010; Mansheim et al. 2017b), if a strong absorption (typical of A stars, where hydrogen absorption is the strongest) is observed and no tracers of on-going star formation are found (Couch & Sharples 1987). Recently, Wu et al. (2018) found that $H\delta$ equivalent width correlates with stellar mass, with more massive galaxies having weaker $H\delta$ absorption lines, but have no study on the impact of environment (see also e.g. Siudek et al. 2017 for a similar result on passive galaxies). Finally, a measure of the flux break at 4000 \AA ($D4000$ and D_n4000 , as defined by Bruzual 1983 and Balogh et al. 1999, respectively), traces the age of the galaxy and also the stellar metallicity (especially for older systems) to a lesser degree. This break is produced by a combination of metal absorption on the atmosphere of old and cool stars and the lack of flux from young and hot OB stars (e.g. Poggianti & Barbaro 1997; Kauffmann et al. 2003) and so it is sensitive to the average age of the stellar population. The 4000 \AA break is also found to be stronger for higher stellar mass galaxies (e.g. Muzzin et al. 2012; Vergani et al. 2008; Hernán-Caballero et al. 2013; Siudek et al. 2017; Wu et al. 2018), hinting at their older stellar populations, in an average sense. In terms of local density, Muzzin

et al. (2012) found that galaxies in cluster environments have on average stronger breaks than their field counterparts at similar stellar masses, which they argue it can be explained by the different fractions of star-forming and quiescent galaxies in different environments.

We aim to investigate the influence of environment on the star formation history of galaxies using a number of spectral indicators (e.g. Balogh et al. 1999; Poggianti et al. 1999, 2009; Dressler et al. 2004; Vergani et al. 2010; Mansheim et al. 2017a; Wu et al. 2018). Due to the spectral coverage of the VIMOS Spectroscopic Survey of a Superstructure in the COSMOS field (VIS³COS, Paulino-Afonso et al. 2018, hereafter PA18) we estimate the current and past star formation activity of galaxies using a combination of [OII] (tracing on-going star formation in moderate to high star-forming galaxies, $\lesssim 10$ Myr), H δ (probing star formation on intermediate timescales - 50 Myr to ~ 1 Gyr prior to observation), and D_n4000 (probing the star formation history on longer timescales). We investigate this using spectroscopic observations of ~ 500 galaxies in and around a superstructure at $z \sim 0.84$ in the COSMOS field (Sobral et al. 2011, PA18) by probing a wide range of environments and stellar masses with a single survey.

This paper is organized as follows: in Section 2 we briefly explain the survey and give some details on the data used. Section 3 details the stacking methods and the spectroscopic measurements. In Section 4 we present the results from individual and stacked spectral properties. We discuss our findings in Section 5. Section 6 where presents the conclusions of our study. We use AB magnitudes (Oke & Gunn 1983), a Chabrier (Chabrier 2003) initial mass function (IMF), and assume a Λ CDM cosmology with $H_0=70$ km s⁻¹Mpc⁻¹, $\Omega_M=0.3$ and $\Omega_\Lambda=0.7$. The physical scale at the redshift of the superstructure ($z \sim 0.84$) is 7.63 kpc''.

2. The VIS³COS survey

The VIS³COS survey maps a large $z \sim 0.84$ over-density spanning $21' \times 31'$ (9.6×14.1 Mpc²) in the COSMOS field (Scoville et al. 2007) with the VIMOS instrument mounted on the VLT. This structure contains three confirmed X-ray clusters (Finoguenov et al. 2007) and also harbours a large-scale over-density of H α emitters (Sobral et al. 2011; Darvish et al. 2014). The full description of the data and redshift measurements are presented in PA18, and we briefly describe here some details.

Our primary targets were selected from the Ilbert et al. (2009) catalogue and with $0.8 < z_{\text{phot},1} < 0.9$ (with $z_{\text{phot},1}$ being either the upper or lower 99% confidence interval limit for each source) and $i_{\text{AB}} < 22.5$. To effectively fill the masks we also add as secondary targets galaxies down to $i_{\text{AB}} < 23$ and with photometric redshifts in the interval $0.6 < z < 1.1$. For the selected targets we obtained high-resolution spectra with the VIMOS High-Resolution red grism (with the GG475 filter, $R \sim 2,500$). This grism covers the 3400 – 4600 Å rest-frame at the redshift of the target superstructure. The observational configuration of the survey was done so we could measure spectral features such as [OII] $\lambda 3726, \lambda 3729$ (partially resolved doublet), the 4000 Å break, and H δ for the superstructure members. We have compared our spectroscopic sample with a mass-complete catalogue and correct for sample incompleteness following the procedure detailed in Section 2.1.

We measure the redshifts of our sources using SPECPRO (Masters & Capak 2011) on the extracted 1D spectra and using a combination of [OII], H+K absorption, G-band, some Fe lines, and H δ . All spectra were visually inspected for the features aforementioned. We obtain secure spectroscopic redshifts for 696 sources

with high S/N, of which 490 are at $0.8 < z < 0.9$. Spectroscopic failures are related to either low S/N continuum or the lack of apparent features.

With the knowledge of the spectroscopic redshift, we improve the estimate of physical parameters that are available in the COSMOS2015 photometric catalogue (Laigle et al. 2016). We ran MAGPHYS (da Cunha et al. 2008) with spectral models constructed from the stellar libraries by Bruzual & Charlot (2003) and using photometric bands from near-UV to near-IR. The dust is modelled following the prescription described by Charlot & Fall (2000). We obtain estimates for the stellar masses and star formation rates for 466 out of the 490 galaxies that are observed at $0.8 < z < 0.9$. Galaxies with no estimates are mostly fainter i -band secondary sources with no match in COSMOS2015 or are not included in the latter catalogue due to different selection bands. Comparing our spectroscopic redshifts with the photometric redshifts of the COSMOS2015 catalogue we find a dispersion $\sigma_{\Delta z/(1+z)} = 0.009$. The scatter in stellar mass and SFR for galaxies with $|z_{\text{spec}} - z_{\text{phot}}| < 0.1$ is ~ 0.15 dex and ~ 0.6 dex respectively. For this study, we use SED derived SFRs since the observed [OII] emission is a poor tracer of SFR for red, low SFR galaxies (with non-detections in quiescent sources) and depends on gas-phase metallicity (e.g. Kewley et al. 2004; Yan et al. 2006; Kocevski et al. 2011) and we have no independent way to quantify dust extinction or measure metallicity from our spectral coverage. We note that there are inevitably issues and limitations affecting SED derived SFRs (especially when young stellar populations dominate galaxies, see e.g. Wuyts et al. 2011), but those affect mostly high SFR galaxies ($> 50 M_\odot \text{yr}^{-1}$), which is a small portion ($< 13\%$) of our sample. We refer to PA18 for a comparison between SED and [OII] derived SFRs for our sample.

Our final sample is restricted to be at $0.8 < z < 0.9$ to match our primary selection (see PA18) and has a total of 466 galaxies spanning a large range of environments across several Mpc. We show in Fig. 1 the colour-magnitude diagram ($r-z$ versus z -band, corresponding roughly to rest-frame $U - V$ vs. V) and the stellar mass-SFR relation from our sample and compare it to the parent photometric catalogue. We note that our sample becomes close to a stellar-mass complete sample at stellar masses greater than $10^{10} M_\odot$.

To estimate the local galaxy over-density we use the density fields computed by Darvish et al. (2015b, 2017). These results are based on the photometric redshift catalogue in the COSMOS field provided by Ilbert et al. (2013). The density field was calculated for a ~ 1.8 deg² area using a mass-limited ($\log_{10}(M/M_\odot) > 9.6$) sample at $0.1 < z_{\text{phot}} < 1.2$. In this paper we define as over-density

$$1 + \delta = \frac{\Sigma}{\Sigma_{\text{median}}} \quad (1)$$

with Σ_{median} being the median of the density field of a specific redshift slice. We used an adaptive kernel with variable size, with small kernel size for crowded regions and larger kernel size for sparser regions, around a typical width of 0.5 Mpc (characteristic size of X-ray clusters, see e.g. Finoguenov et al. 2007). We note that re-computing the density field using the spectroscopic redshifts from our sample does not significantly change the underlying density fields. For a more detailed description of the method, we refer to Darvish et al. (2015b, 2017). Having a pure density-based definition of the environment does not translate exactly into different physical regions (see e.g. Aragón-Calvo et al. 2010; Darvish et al. 2014). In each density bin we can have a mix of different regions, i.e.

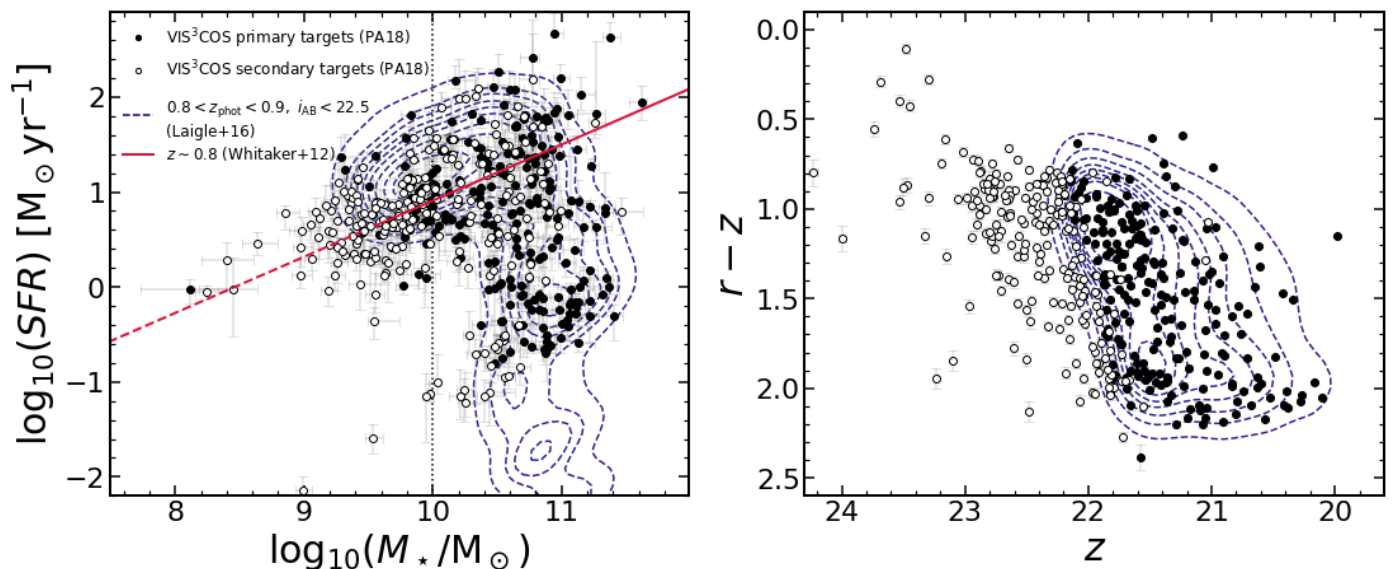


Fig. 1. Stellar masses and star formation rates derived from SED fitting in our spectroscopic sample at $0.8 < z < 0.9$, showing the primary (filled circles) and secondary (open circles) targets separately (left). Colour-magnitude diagram for the same sample (right). For comparison, we show the derived best-fit relation for star-forming galaxies computed at $z = 0.84$ using the equation derived by Whitaker et al. (2012) over a large average volume in the COSMOS field (the dashed line is an extrapolation below their stellar mass completeness). The vertical dotted line shows the approximate stellar-mass representativeness limit of our survey. The dotted contours show the COSMOS2015 distribution of galaxies with $0.8 < z_{\text{phot}} < 0.9$ and $i_{\text{AB}} < 22.5$ from 10% to 90% of the sample in 10% steps.

dense filamentary structures can have similar local densities as the core of rich galaxy groups or cluster outskirts and small groups could share the same local density as scarcely populated filaments. Nonetheless there are typical densities at which field ($\log_{10}(1 + \delta) \lesssim 0.1$), filament ($0.1 \lesssim \log_{10}(1 + \delta) \lesssim 0.6$), and cluster galaxies ($\log_{10}(1 + \delta) \gtrsim 0.6$) dominate the population (see PA18 for more details).

2.1. Completeness corrections

Due to the nature of spectroscopic surveys, it is hard to observe all galaxies in a field down to a single magnitude or stellar mass limit. To make sure that our final spectroscopic sample is as representative as possible of the global population over the same field, we use the excellent wealth of data available in the COSMOS field to quantify the representativeness of our sample. Specifically, we make use of the COSMOS2015 catalogue which is reported to be mass-complete down to $10^{9.4}M_{\odot}$ for quiescent galaxies at these redshifts (mass-completeness limit is 10^9M_{\odot} if considering all galaxies in the observed region Laigle et al. 2016). In Fig. 2 we show the relative fraction of galaxies in our spectroscopic sample compared to the mass-complete sample from the COSMOS2015 catalogue. When splitting the samples into the star-forming and quiescent populations, we find different incompleteness effects. Our completeness for quiescent galaxies starts to drop at stellar masses below $10^{10.5}M_{\odot}$, and we fail to detect a single quiescent galaxy in the lower stellar mass bin (10^9M_{\odot} - $10^{9.5}M_{\odot}$). For star-forming galaxies our completeness drops at lower stellar masses (below $10^{9.5}M_{\odot}$).

We assign weights to all of our galaxies in our sample based on the position of the stellar-mass, specific SFR and local overdensity with respect to the mass-complete population at $0.8 < z_{\text{phot}} < 0.9$. In practice, we compute the fraction of galaxies observed in the three-dimensional region centred on each target

in the mass-complete catalogue and compare that to the fraction of galaxies in our spectroscopic sample over the same region:

$$w_i = \frac{N_{\text{mass}, R_i}}{N_{\text{spec}, R_i}} \times \frac{N_{\text{spec}}}{N_{\text{mass}}}, \quad (2)$$

where N_{mass} represents the numbers of galaxies in the complete mass catalogue, N_{spec} is the number of galaxies in the spectroscopic catalogue, and the index R_i means the variable is computed inside the region surrounding galaxy i . To define each region we use an ellipsoidal selection on the three-dimensional space with a size of 0.25 in the $\log_{10}(M_{\star}/M_{\odot})$ dimension, 1 in the $\log_{10}(s\text{SFR})$ dimension and 0.5 in the $\log_{10}(1 + \delta)$ dimension.

We expect these corrections to be valid for all galaxies above 10^9M_{\odot} which is the quoted mass-completeness limit for star-forming galaxies at these redshifts (Laigle et al. 2016). However, since our primary selection would translate to a limiting mass (considering all galaxies) of approximately $10^{10}M_{\odot}$ (this is the median stellar mass of all $22.3 < i_{\text{AB}} < 22.7$ and $0.8 < z_{\text{phot}} < 0.9$ galaxies in the COSMOS2015 catalogue) and that is reflected in the low completeness values at those stellar masses (see Fig. 2), we restrict our analysis to galaxies above that stellar-mass threshold. Considering the sub-populations of star-forming galaxies, our primary i -band selection translates in different limiting stellar masses. For the star-forming population, our i -band selection would typically select galaxies down to $10^{9.9}M_{\odot}$. For the quiescent population, the same selection would be limited at $10^{10.6}M_{\odot}$. We try to account for this effect by weighting galaxies based on their position in the stellar mass - sSFR plane, which aims to minimize this selection bias.

3. Spectroscopic properties

3.1. Composite spectra

Co-adding spectra of galaxies binned by similar physical properties increase the signal-to-noise ratio and allow for a better

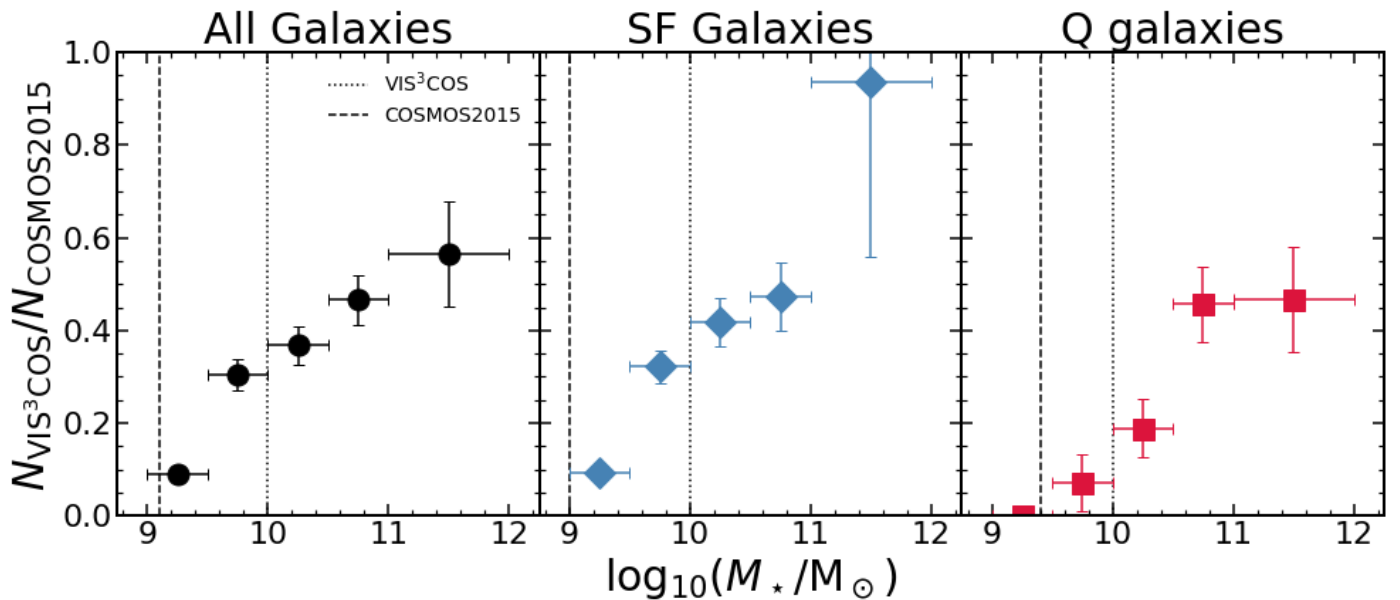


Fig. 2. The number of galaxies with spectroscopic redshifts in VIS³COS divided by the number of galaxies in the mass-complete COSMOS2015 catalogue over the same region and limited to $0.8 < z_{\text{phot}} < 0.9$ for all, star-forming, and quiescent galaxies, respectively. The vertical dashed lines correspond to the mass-complete limits in COSMOS2015. The vertical dotted lines correspond to our quoted limiting mass of $\sim 10^{10} M_\odot$. The error bars are computed from Poisson statistics.

determination of the median spectral properties of the sample in different regions of the parameter space that we aim to probe (e.g. Lemaux et al. 2010). We construct composite spectra by binning in stellar mass, over-density, and star formation rate. For a quick view on the different composite spectra, see Figs. A.1–A.3.

To obtain composite spectra, we first normalize each spectrum to the mean flux measured in the range 4150–4350 Å. Using the redshift we have measured (see Section 2), we linearly interpolate the spectrum onto a common universal grid (3250 – 4500 Å, $\Delta\lambda = 0.5 \text{ \AA pix}^{-1}$). We then compute the median flux at each wavelength in the grid to obtain the final composite spectra. We normalize each spectrum dividing it by the median flux measured at 4150 – 4350 Å. We assign a weight to each spectrum based on the completeness corrections detailed in Section 2.1. Finally, we obtain the composite spectra as the weighted median flux per wavelength bin in the defined grid. We have repeated our analysis using different normalization schemes (blueward of 4000 Å and with no normalization), and our results are qualitatively the same.

3.2. Spectral quantities

To study the star formation history of galaxies, we use three tracers - [OII], H δ , D_n4000 - present in our spectra (e.g. Balogh et al. 1999; Dressler et al. 2004; Oemler et al. 2009; Poggianti et al. 2009; Vergani et al. 2010; Mansheim et al. 2017b). To be consistent with the classical notation, a negative equivalent width corresponds to a line in emission while positive values correspond to a line in absorption.

3.2.1. [OII] emission

To measure the [OII], we fit a double Gaussian to the doublet. The centre of each component is set to be $\lambda_1 = 3726.08 \pm 0.3 \text{ \AA}$ and $\lambda_2 = 3728.88 \pm 0.3 \text{ \AA}$ (a small shift in the line centre is allowed to account for our finite resolution, and we allow for a systematic shift to the doublet to account for redshift uncertainties). We

measure the flux and line equivalent widths by integrating over the best-fit models. For more details we refer the reader to PA18 (see also Fig. 3, left panel).

3.2.2. H δ in emission and absorption

We fit the emission and absorption components of the H δ line by using a double Gaussian fit with two independent components (see Fig. 3, right panel): one forced to have a negative amplitude (for the absorption) and one forced to have a positive amplitude (for the emission). To prevent a set of degenerate model combinations which produce the same combined result but for which the individual components are clearly not physically representative of the observed data ¹ we force the width of the emission line to be always smaller than the absorption component. This is informed by the empirical information from the individual stacks we obtain. To estimate the first guess amplitude of the absorption, we take the minimum of the continuum subtracted spectra. The amplitude of the emission line is computed by first fitting a single Gaussian to the absorption feature (whenever present) masking the $\pm 3 \text{ \AA}$ around the central wavelength, and then taking the maximum of the absorption subtracted spectra. We also assign an initial σ of 4 and 1 Å for the absorption and emission component, respectively. We then measure the line fluxes and equivalent widths from the best-fit models.

3.2.3. Continuum and error estimation

For all line fits we individually define two regions (one blue-ward, one red-ward of the line) with a width of 15 Å width (~ 3 times the spectral resolution) from which we estimate the median continuum level. Then the local continuum is defined as a straight line that goes through those two points (see e.g. Balogh et al. 1999; Lemaux et al. 2010; Mansheim et al. 2017b). To minimize the

¹ The sum of two symmetric components is degenerate against an equal multiplicative factor on the amplitude of individual components.

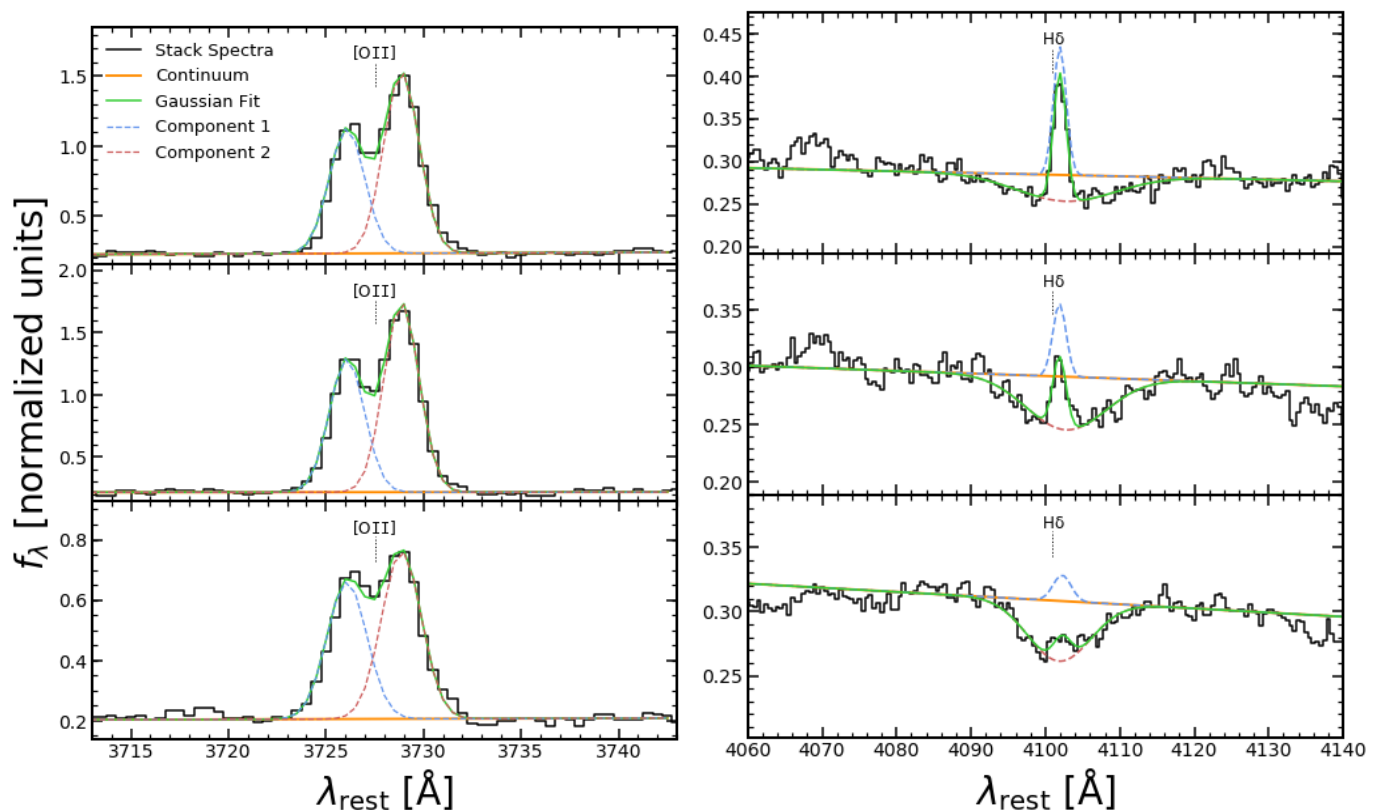


Fig. 3. Three examples of the fit to the stacked [OII] emission (left) and the stacked H δ absorption+emission (right) spectral lines. The solid black line shows the observed spectrum. The green line shows the median fit (after 10,000 realizations) and the orange line the estimated continuum around the line. We also show in red and blue dashed lines the fit of each Gaussian component.

effect of a particular choice of windows from which we compute the continuum, we compute the median flux for 5,000 random shifts of $k\text{Å}$ on the proposed interval, where k is randomly drawn from a normal distribution centred at 0 and with a width of 5Å . Then the final estimate of the continuum is measured from the median of the 5,000 realizations.

To estimate the errors on the derived spectral quantities, we have performed a bootstrap sampling of each sub-sample of spectra. This method allows us to estimate the variance occurring within each sub-sample. This quoted error is always larger than the formal uncertainties from the fit. We perform the fit on 1,000 individual bootstrapped spectra (using only 80% random galaxies drawn from the sub-sample) and derived the final errors from the 16th and 84th percentiles of the distribution of best-fit values.

3.2.4. 4000 Å break

Apart from line measurements, we have also computed the strength of the break at 4000vÅ (D_{4000} and D_n4000 defined by Bruzual 1983; Balogh et al. 1999, respectively). We automated the computation of these quantities by integrating the spectra over the red (D_{4000} : $4050\text{--}4250\text{Å}$, D_n4000 : $4000\text{--}4100\text{Å}$) and blue (D_{4000} : $3750\text{--}3950\text{Å}$, D_n4000 : $3850\text{--}3950\text{Å}$) intervals and computing the ratio of those fluxes as

$$X_{4000} = \frac{\int_{\lambda_{r1}}^{\lambda_{r2}} f_{\nu} d\lambda}{\int_{\lambda_{b1}}^{\lambda_{b2}} f_{\nu} d\lambda}, \quad (3)$$

where X is either D or D_n depending on the integration limits of the red (λ_{ri}) and blue (λ_{bi}) intervals. When comparing both indices, we find them to correlate well, with a median difference of $< 1\%$ and a spread of 30% on individual measurements. We opt to use for the remainder of the paper the value of D_n4000 since it should be less affected by errors due to Poisson sampling and less affected by reddening (Balogh et al. 1999). Nevertheless, our results are qualitatively the same regardless of which index we use. To avoid the contamination by emission lines in the integrated regions we mask 6Å regions around the [NIII] and H ζ lines (see e.g. Fig. A.1).

3.3. Stellar population age estimates

Estimating a single representative stellar age for galaxies is not a trivial task due to the expected variety of their star formation histories. Nonetheless, we can obtain an estimate given a few sets of assumptions. We will use the D_n4000 index as a proxy for age and obtain an estimate from a set of stellar population models described by Bruzual & Charlot (2003). We attempt to estimate an age based on a single stellar population (SSP), with the notation t_{SSP} , which should trace the age of the last major burst that the galaxy had.

We note that the D_n4000 index depends not only on age but also on the stellar metallicity, especially for ages greater than 1 Gyr (e.g. Bruzual 1983; Poggianti & Barbaro 1997; Balogh et al. 1999). Since we do not have any independent way to estimate stellar metallicity for all galaxies, we need to make a few assumptions to try and mitigate possible bias in our interpretations. We assume that our sample follows the stellar mass-metallicity

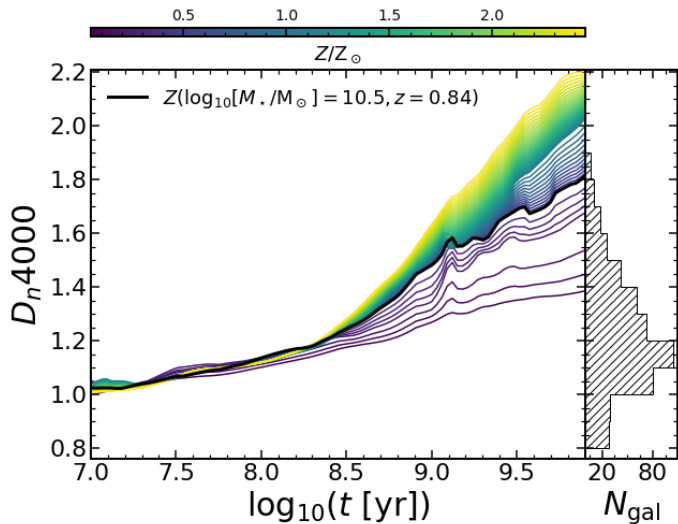


Fig. 4. The value of D_n4000 as a function of stellar age for a set of single stellar population models from Bruzual & Charlot (2003) for different stellar metallicities from $Z = 0.1Z_\odot$ to $Z = 2.5Z_\odot$. The thick solid line shows the relation using the stellar metallicity for the median stellar mass and redshift of our sample (see Section 3.3). On the right panel, we show the distribution of measured D_n4000 values for the galaxies in our sample.

relation that is found locally and up to $z \sim 1$ (e.g. Tremonti et al. 2004; Gallazzi et al. 2005; Savaglio et al. 2005; Zahid et al. 2011, 2013; Ma et al. 2016; De Rossi et al. 2017; Leethochawalit et al. 2018). We then estimate individual stellar metallicities based on a recent numerical simulation study by Ma et al. (2016) which parametrizes stellar metallicity as a function of stellar mass and redshift as:

$$\log_{10} \left(\frac{Z_\star}{Z_\odot} \right) = 0.40 \left[\log_{10} \left(\frac{M_\star}{M_\odot} \right) - 10 \right] + 0.67e^{-0.5z} - 1.04. \quad (4)$$

For a stellar mass ($10^{10.5}M_\odot$) and redshift ($z = 0.84$) of our sample we determine a stellar metallicity of $Z_\star \sim 0.008 = Z_\odot/2.5$. For a stellar mass of $10^{11.5}M_\odot$ we get $Z_\star \sim 0.02$ and for a stellar mass $10^{9.5}M_\odot$ we get $Z_\star \sim 0.003$. We show in Fig. 4 the age dependence of D_n4000 for different stellar metallicities spanning the expected range of our sample.

To estimate the age of a galaxy (or group of galaxies) we first compute the individual (or median) stellar metallicity and then use the D_n4000 -age relation for an SSP based on Bruzual & Charlot (2003) models at that metallicity to derive the stellar age. The errors on the SSP ages are derived as detailed in Section 3.2.3 and do not include any uncertainty on the metallicity.

4. Results

We explore the results on the spectral properties of our galaxies at $0.8 < z < 0.9$, highlighting both composite spectra and individual galaxies in this section. We aim to probe the influence of key physical properties (stellar mass, environment, and SFR) on the median observed spectral properties of our sample. We note that for H δ we have insufficient S/N on most galaxies to get robust measurements and we refrain from discussing that spectral feature in terms of individual galaxies.

We summarize in Fig. 5 (see also Appendix A and Table A.1) the properties of composite spectra on [OII] and H δ (both

emission and absorption) line equivalent widths and D_n4000 at different stellar masses, over-densities, and SFRs. We stress that for samples not selected in stellar mass, we impose a minimum stellar mass limit of $10^{10}M_\odot$.

4.1. Global trends on the spectroscopic properties

4.1.1. Stellar mass

We discuss here the trends of the measured spectroscopic properties as a function of the stellar mass. While we show in Fig. 5 the results at stellar masses between 10^9M_\odot and $10^{10}M_\odot$, we do not discuss them as this results suffer from high incompleteness (see Section 2.1).

In terms of the [OII] line equivalent width ($EW_{[OII]}$), we find in Fig. 5 a strong decrease with stellar mass, by a factor of ~ 3 in strength from the lowest ($10 < \log_{10}(M_\star/M_\odot) < 10.5$) to the highest stellar mass bin ($\log_{10}(M_\star/M_\odot) > 11$), which points to a decrease in sSFR with increasing stellar mass from $\sim 10^{-9}\text{yr}^{-1}$ to $\sim 10^{-10}\text{yr}^{-1}$ (a consequence of the main sequence of star-forming galaxies, see also Darvish et al. 2015a). We compare the results for individual galaxies and composite spectra with others available in the literature (Bridge et al. 2015; Cava et al. 2015; Darvish et al. 2015a). Our results are broadly consistent (in terms of the observed trends) with the literature which find a decrease in the absolute line equivalent width with increasing stellar mass. However, we find some discrepancies with Cava et al. (2015) and Bridge et al. (2015) in terms of the average value in bins of stellar mass that are likely related to the target selection in each work. In the case of Cava et al. (2015) they report consistently higher values of [OII] line equivalent width. However, their sources are selected through medium band filters down to equivalent widths of $\sim 15\text{-}20 \text{ \AA}$, which naturally explains their higher median values. As for the case of Bridge et al. (2015) they study a large field with blind spectroscopy, and they exclude large equivalent width ($EW \gtrsim 40 \text{ \AA}$) galaxies to avoid contamination by higher redshift interlopers (Ly α emitters), which can explain their observed lower equivalent widths. We find $EW_{[OII]}$ values consistent with Darvish et al. (2015a), which had a similar observational setup as the VIS³COS survey.

In the middle panels of Fig. 5 we show the measured equivalent width of the H δ emission and absorption for all composite spectra which allowed a measurement (some of them did not show any signs of absorption). The H δ absorption line equivalent width decreases with increasing stellar mass (from $EW_{H\delta} = 2.7 \pm 0.2 \text{ \AA}$ at $10 < \log_{10}(M_\star/M_\odot) < 10.5$ down to $EW_{H\delta} = 1.1^{+0.3}_{-0.2} \text{ \AA}$ at $\log_{10}(M_\star/M_\odot) > 11$). The H δ emission line equivalent width also correlates with stellar mass with stronger emission being found at lower stellar masses, dropping from $EW_{H\delta} = -0.6^{0.3}_{-0.2} \text{ \AA}$ at $10 < \log_{10}(M_\star/M_\odot) < 10.5$ to a marginally non-existent emission component with $EW_{H\delta} = -0.1 \pm 0.1 \text{ \AA}$ at $\log_{10}(M_\star/M_\odot) > 11$. When compared to the results by Wu et al. (2018) we see that there is also a decrease on their reported equivalent width with stellar mass but at a steeper rate. We attribute the discrepancies to the different methods used to compute the line equivalent width. They use a spectral index defined by Worthey & Ottaviani (1997) which measures the line equivalent width on an emission subtracted/masked spectrum. We also show the dependence of the emission to absorption ratio of the equivalent widths as a proxy for the ratio of O to A stars. Our results are consistent with no dependence on stellar mass.

The bottom panels of Fig. 5 show the dependence of the 4000 \AA break strength on the same quantities mentioned above. We find

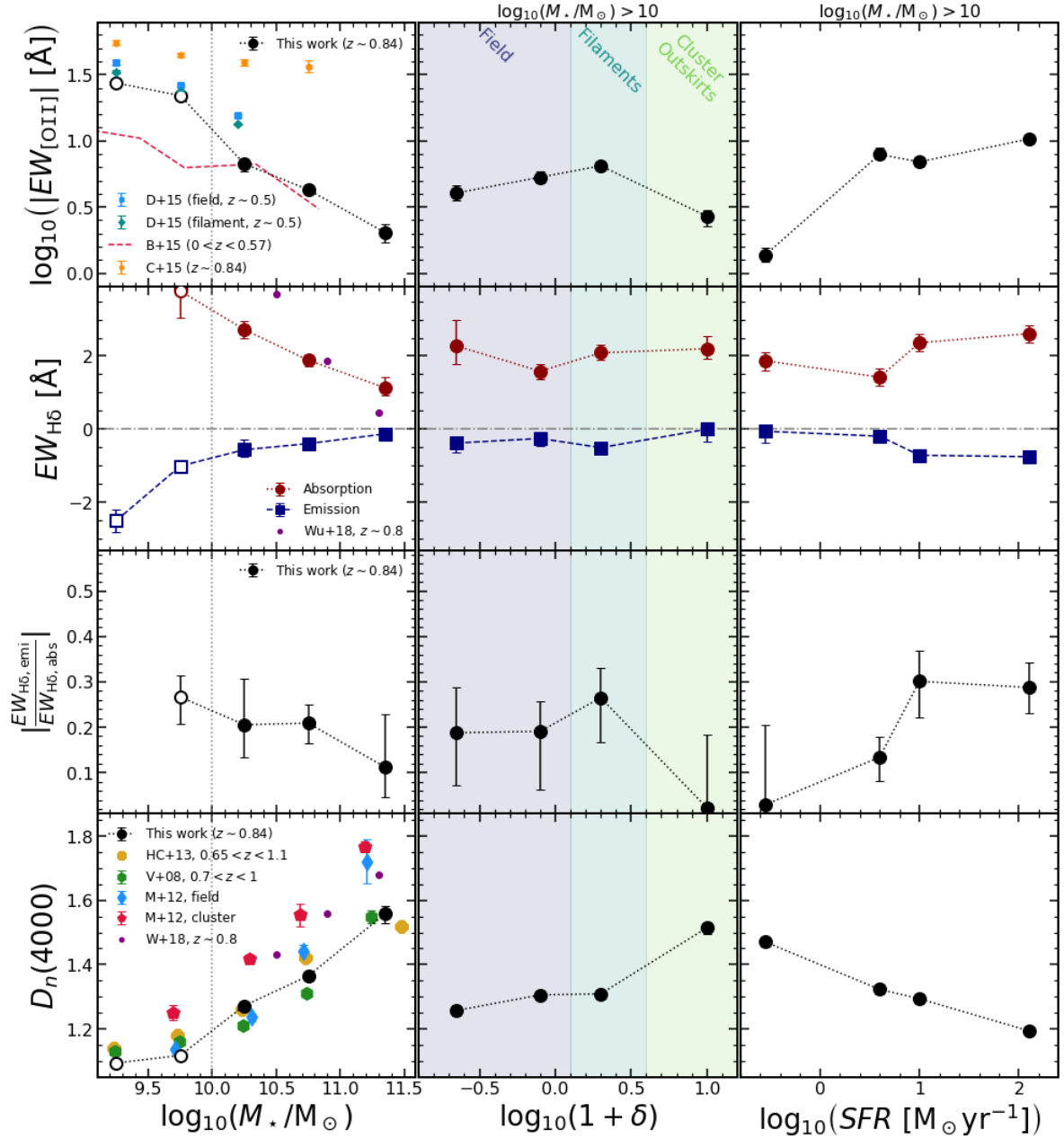


Fig. 5. The dependence of the three spectral features detailed in Section 3.2 (from top to bottom - [OII] equivalent width, H δ equivalent widths, and $D_n(4000)$) as a function of stellar mass (left), over-density (middle), and SED-derived SFR (right). We show our stellar mass representativeness limit as a vertical dotted line in the left panels and show as empty symbols the measurements for which the completeness effects are large. We note that for bins not defined in stellar mass (middle and right panels), the composite spectra are built from galaxies with stellar mass greater than $10^{10} M_{\odot}$. Results from this paper are shown as large and dotted line connected symbols with associated error bars derived from the 16th and 84th percentiles of the 1,000 bootstrapped fits (if the error bars are not seen, it implies an error smaller than the symbol size). When looking at trends with stellar mass, we see a decrease in [OII] and H δ emission (blue squares) and absorption (red circles) strength and an increase of the average age of the stellar population (traced by $D_n(4000)$). For trends with over-density, there is a peak in [OII] equivalent width at filament-like densities and H δ equivalent widths show little dependence on local density. There is also a clear trend for galaxies being older in higher density regions. Lastly, both [OII] and H δ strength increase with SFR (excluding the most star-forming galaxies) and we see younger populations in galaxies with higher SFR, as expected. We compare our results to other surveys in the literature (Bridge et al. 2015; Darvish et al. 2015a; Cava et al. 2015; Wu et al. 2018; Hernán-Caballero et al. 2013; Vergani et al. 2008; Muzzin et al. 2012). For a more detailed discussion on the differences we refer to Sections 4.2.1 and 4.2.2.

a strong correlation between $D_n(4000)$ and stellar mass, increasing from $D_n(4000) = 1.27^{+0.02}_{-0.01}$ at $10 < \log_{10}(M_{\star}/M_{\odot}) < 10.5$ to $D_n(4000) = 1.56 \pm 0.03$ at $\log_{10}(M_{\star}/M_{\odot}) > 11$. This trend points to more massive galaxies also having the older stellar populations. Our results are in general agreement with other studies in the literature targeting either clustered regions (GCLASS - Muzzin

et al. 2012) or large field surveys (VVDS, SHARDS, LEGA-C - Vergani et al. 2008; Hernán-Caballero et al. 2013; Wu et al. 2018, respectively). The trend with stellar mass is seen in all surveys. We find median values in between the quoted average/median of other studies in the literature at similar redshifts. We find lower median $D_n(4000)$ at fixed stellar masses with respect to values reported by

Muzzin et al. (2012) for cluster galaxies, which is expected given the dependence of D_n4000 seen with the environment and the fact that we are probing a majority population at lower densities than the cluster sample. This is consistent with what we find when splitting the sample in stellar mass and local density bins, with galaxies at fixed stellar mass having the stronger 4000 Å breaks at the higher densities we probe (see Section 4.2).

4.1.2. Local environment

Our analysis is restricted to stellar masses greater than $10^{10}M_\odot$ and for this sub-sample there is little variation in the median stellar mass across the different bins ($\Delta \log_{10}(M_\star/M_\odot) < 0.15$). We find that the absolute value of $EW_{[\text{OII}]}$ increases from $4.0^{+0.5}_{-0.6}$ Å to $6.5^{+0.4}_{-0.5}$ Å from field to filament-like densities and then drops to $2.7^{+0.5}_{-0.3}$ Å in our highest density bin. This is pointing to a slight increase of the sSFR at filament-like densities for galaxies more massive than $10^{10}M_\odot$ and then a strong drop towards the higher density regions probed here. We also compared the trends with local density to those with environmental regions (field, filament, and cluster, see Table A.1) as defined in PA18 (see also Darvish et al. 2015b, 2017) and find a decline of $|EW_{[\text{OII}]}|$ from field to filament to cluster regions (from $4.6^{+0.5}_{-0.4}$ Å to $4.4^{+0.3}_{-0.4}$ Å to 3.4 ± 0.5 Å, respectively), for galaxies more massive than $10^{10}M_\odot$. These differences reflect the nuances of using different tracers of the galactic environment, but both reinforce a drop of $EW_{[\text{OII}]}$ towards the denser regions studied here.

Regarding the H δ absorption line, we find results that are consistent with no trend with local density. For H δ emission, all our derived values for galaxies more massive than $10^{10}M_\odot$ are also consistent with no dependence with over-density, having measured equivalent widths around ~ 0 -0.5 Å. We find no significant dependence on over-density on the results regarding the ratio between absorption and emission of H δ , given our error bars.

Finally, we find an increase of D_n4000 towards higher densities. In low- to intermediate-density regions ($\log_{10}(1 + \delta) < 0.5$) we find $D_n4000 \sim 1.26 - 1.31$ (corresponding to an SSP age of $\sim 0.35 - 0.47$ Gyr). The strength of the 4000 Å break then increases at higher densities ($\log_{10}(1 + \delta) > 0.5$), reaching $D_n4000 = 1.51 \pm 0.02$ (corresponding to an SSP age of $\sim 1.1 \pm 0.1$ Gyr).

4.1.3. Star formation rate

Our analysis is restricted to stellar masses greater than $10^{10}M_\odot$, which probes a range of 3 dex in SFR. We note that the difference in the median/mean stellar mass in each defined SFR bins is smaller than 0.1 dex, so the correlations of the studied tracers with SFR are not affected by an underlying SFR-stellar mass relation. This happens since at stellar masses $> 10^{10}M_\odot$ there is a large spread in star-formation rates due to existing star-forming and quiescent galaxies of similar stellar mass. Overall, there is an increase of $EW_{[\text{OII}]}$ with increasing SFR. We find a strong increase from the quiescent (low-SFR) population (-1.4 ± 0.2 Å for $\log_{10}(SFR) < 0.4$) to the active (intermediate-SFR) star-forming population (~ 7.5 Å) in our sample. Then we find a small increase towards the high-SFR population (-10.3 ± 0.5 Å for $\log_{10}(SFR) > 1.2$).

Concerning the H δ absorption component, we find a small increase of the equivalent width with SFR, from $EW_{H\delta} \approx 1.9 - 1.4 \pm 0.25$ Å at $\log_{10}(SFR [M_\odot \text{yr}^{-1}]) < 0.8$ to $EW_{H\delta} \approx 2.4 -$

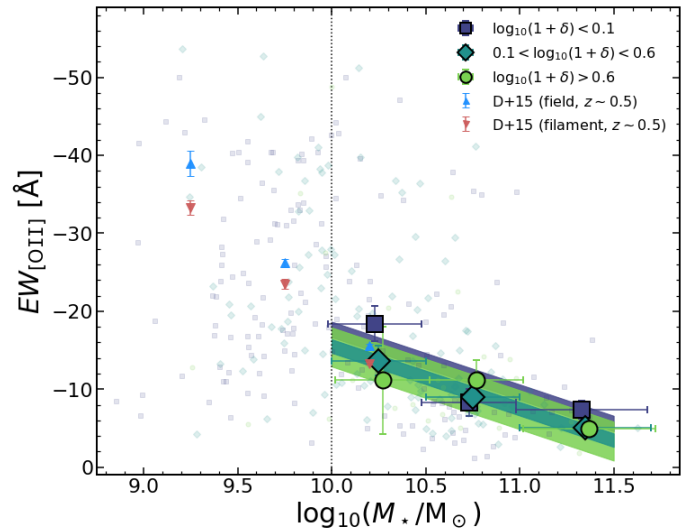


Fig. 6. We show the relation between [OII] equivalent width and stellar mass for the [OII]-emitters in our sample in three different bins of over-density. We compare our results (large green and dark blue symbols are the median of the population, and the same smaller symbols represent individual measurements) with results from Darvish et al. (2015a) of filament/field galaxies, as small red/blue triangles, respectively. We show the best fit (with error estimate) from Eq. 5 for each density bin as shaded regions. We show that higher stellar mass galaxies have weaker [OII] emission and this relation is seen in all over-density subsets.

2.6 ± 0.25 Å at $\log_{10}(SFR [M_\odot \text{yr}^{-1}]) > 0.8$. The H δ emission shows a correlation with SFR that mirrors what we find with [OII] emission with the line strength increasing from low to high SFRs (from $-0.1^{+0.1}_{-0.3}$ Å to -0.8 ± 0.1 Å). The emission to absorption line ratio is marginally consistent with no trend with SFR (though we see a rise on the median value from low to intermediate-high SFR galaxies).

Finally, we observe a steady decrease in the value of D_n4000 from the lowest SFR bin ($D_n4000 = 1.47 \pm 0.01$ for $\log_{10}(SFR [M_\odot \text{yr}^{-1}]) < 0.4$) to the highest SFR bin ($D_n4000 = 1.19 \pm 0.01$ for $\log_{10}(SFR [M_\odot \text{yr}^{-1}]) > 1.2$). This is consistent with what is expected from the evolution of galaxies, since we expect a larger fraction of young stars in highly star-forming galaxies which decreases the value of D_n4000 .

4.2. Disentangling environment and stellar mass effects

To disentangle the effects of stellar mass and environment, we have explored our sample binned both in stellar mass and over-density bins. We chose the over-density bins in a way that they should be representative of field (low-density), filament (intermediate density), and cluster outskirts (high-density) regions (see PA18 for more details). We show for individual galaxies and composite spectra the influence of over-density in the observed spectroscopic properties in three different bins of stellar mass (chosen as a compromise for reasonable S/N for H δ).

4.2.1. $EW_{[\text{OII}]}$

We show in Fig. 6 the relation between [OII] line equivalent width and stellar mass for individual galaxies with an [OII] detection, which should mainly trace star-forming galaxies, though we find a $\sim 10\%$ contamination (17 out of 166 [OII] emitters) in our $> 10^{10}M_\odot$ sample from low sSFR ($\log_{10}(sSFR) < -11$) galaxies (see also e.g. Yan et al. 2006; Lemaux et al. 2010). We attempt to

separate the effects of local density on this correlation and find that the correlation between [OII] line equivalent width and stellar mass is similar in all environments. We find similar gradients at all environments and fit a linear relation with a fixed slope (the average of individually fitted slopes)² for all environments:

$$EW_{[\text{OII}]} = 8.05 \times \log_{10} \left(M_{\star} / 10^{10} M_{\odot} \right) + b. \quad (5)$$

The best fit values are shown in Table 1. Line equivalent widths should be insensitive to dust if both continuum and line flux are being emitted from the same regions. We note, however, that there is a different attenuation of stellar and nebular emission seen in the local Universe (e.g. Calzetti et al. 2000; Wild et al. 2011), which seems to be less pronounced at higher redshifts ($z \gtrsim 1$, e.g. Kashino et al. 2013; Pannella et al. 2015). We tentatively find a lower [OII] equivalent width with increasing density, but all relations are within 1σ uncertainties. This is consistent with no dependence of the sSFR with environment for a star-forming population (e.g. Muzzin et al. 2012; Koyama et al. 2013; Darvish et al. 2016; PA18).

Concerning the results from composite spectra, we show in Fig. 8 an overall trend [OII] line equivalent width with stellar mass (as reported in Fig. 6) at each over-density bin. We show that [OII] depends on both the stellar mass and environment of galaxies. For lower stellar mass galaxies ($10 < \log_{10}(M_{\star}/M_{\odot}) < 10.5$) we find a small decrease in $EW_{[\text{OII}]}$ with increasing local density. Intermediate-mass galaxies ($10.5 < \log_{10}(M_{\star}/M_{\odot}) < 11$) show a small rise (at the 1.7σ level) in $EW_{[\text{OII}]}$ from field to filament-like regions and then a small decrease towards cluster-like regions. The most massive galaxies are consistent with no environmental effect on the [OII] emission. The local density dependence of the $EW_{[\text{OII}]}$ emission in the stacked spectra can be reconciled with the apparent environmentally-independent estimates we show in Fig. 6. We include in the stacking analysis all the galaxies with no [OII] emission (either quiescent or dusty) which are known to be more common in higher density regions (quiescent - e.g. Peng et al. 2010b; Cucciati et al. 2010; Sobral et al. 2011; Muzzin et al. 2012; Darvish et al. 2016; PA18; dusty star formation - e.g. Smail et al. 1999; Gallazzi et al. 2009b; Koyama et al. 2013; Sobral et al. 2016).

4.2.2. 4000 Å break

The 4000 Å break is a proxy for the age of the underlying stellar population (see Section 3.3). Under that assumption we find that at higher masses ($\log_{10}(M_{\star}/M_{\odot}) > 10$) galaxies residing in high-density regions are typically older than their counterparts at lower density regions. We find that D_n4000 is $5 \pm 3\%$ (lower stellar mass, ~ 0.3 Gyr difference) to $23 \pm 6\%$ (higher stellar mass, ~ 2 Gyr difference) higher in high-density regions when compared to lower density regions, see Fig. 7. There is also an underlying correlation between stellar mass and D_n4000 , with more massive galaxies having stronger flux breaks at 4000 Å, thus being older (rising from ~ 1.1 to $\sim 1.35 - 1.65$ from lower to higher stellar masses, see also e.g. Vergani et al. 2008; Muzzin et al. 2012; Hernán-Caballero et al. 2013; Wu et al. 2018).

The relative difference between field and cluster galaxies shown by Muzzin et al. (2012) indicates a stronger break in higher density regions, although, in their sample, the difference

between cluster and field galaxies becomes smaller with increasing stellar mass. This can be interpreted as a stronger dependence of the quenched fraction on environment for lower stellar masses (e.g. Peng et al. 2010b) which is less evident at $z \sim 1$ (Muzzin et al. 2012; Darvish et al. 2016 though we do find a dependence for our sample, see PA18). However, one also needs to account for the different timescales of the tracer used to defined quiescence (we use the SED-based sSFR, which traces the past ~ 100 Myr) and D_n4000 which traces the average age of the stellar population (and can range from several hundreds of Myr to several Gyr, see e.g. Section 4.3 where we show that quiescent galaxies in high-density environments have larger D_n4000 when compared to the quiescent population in low-density regions).

We also note that the separation between field and cluster galaxies in Muzzin et al. (2012) is done by using the cluster-centric radius (defined as the distance to the brightest cluster galaxy of each of their clusters). Their field sample is representative of a population of galaxies in-falling into the clusters, and their cluster galaxies are drawn from a sample of rich clusters. This means that making a direct comparison is not straightforward. Thus we find that their field galaxies should correspond to filament-like densities as defined in our paper and cluster galaxies likely correspond to higher densities than what we probe with the VIS³COS survey. Nonetheless, the quiescent fraction that is reported in Muzzin et al. (2012) is in line with that found in studies where field samples are independent of cluster regions and do not reach rich cluster density regions (van der Burg et al. 2013; Peng et al. 2010b). It is therefore not clear that the definition of field and cluster samples can explain the observed differences in the differential trend of D_n4000 and stellar mass for field and cluster galaxies.

Quantifying the rate of increase of D_n4000 with the linear model (we fix the y-intercept to the average of individual fits)³

$$D_n4000 = m \times \log_{10} \left(M_{\star} / 10^{10} M_{\odot} \right) + 1.15, \quad (6)$$

where the best fit values are summarized in Table 1.

We confirm more clearly the trend reported on individual galaxies when looking at D_n4000 in the composite spectra (see Fig. 8). At fixed density, we see that D_n4000 increases from low to high stellar masses. At fixed stellar mass, we find that D_n4000 increases from low to high-density environments (with the exception at the highest densities where galaxies between $10^{10} M_{\odot}$ and $10^{11} M_{\odot}$ have similar values of D_n4000). We also find that the difference between different stellar mass bins is different for different density regions. The relation becomes steeper at intermediate densities when compared to the low-density regions probed here. At the higher densities we probe, the difference between the low and intermediate stellar mass bins is smaller, but we find a larger difference towards the highest stellar masses. This points to both stellar mass and environment having an impact on the stellar populations of galaxies, with higher density environments harbouring older galaxies at all stellar masses.

4.2.3. H δ emission and absorption

We also find a dependence on the stellar mass of the strength of the H δ emission with lower stellar mass galaxies having on average higher equivalent widths (see Fig. 8, Table A.1). Within

² We made this choice since individual values for the slope are found to be similar and within the reported errors, and by doing so we can report the change in normalization independent of the slope of the relation.

³ We made this choice since individual values for the y-intercept are within the reported errors, and by doing so we can report the change in gradient independent of the normalization of the relation.

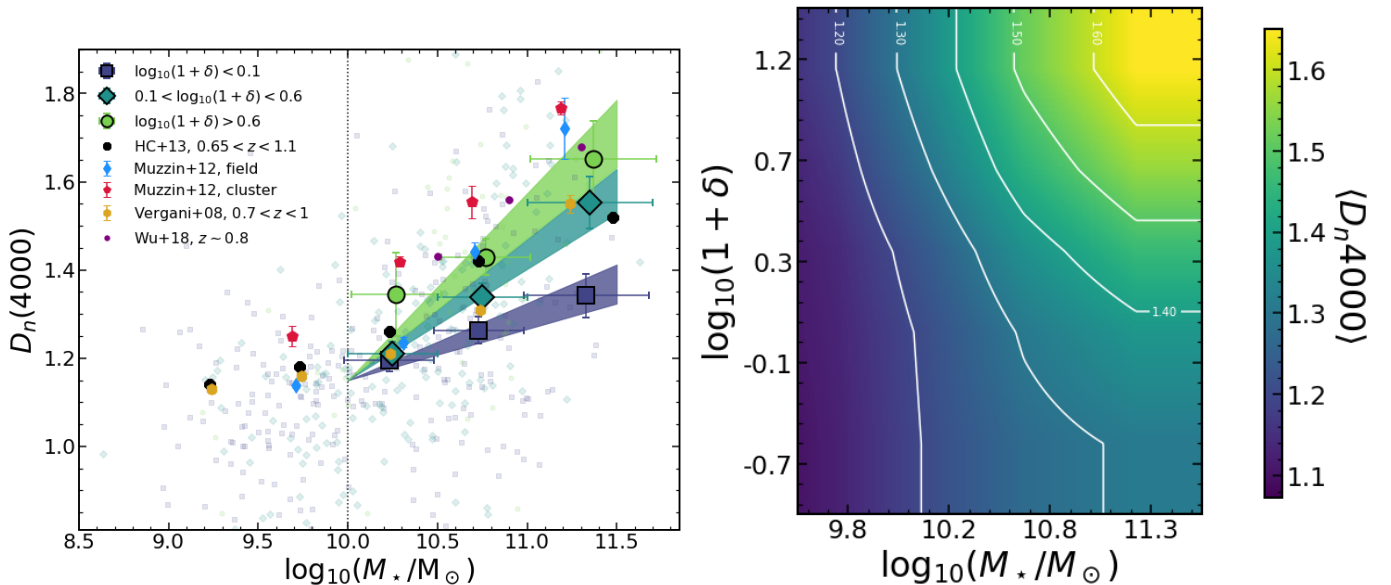


Fig. 7. D_n4000 as a function of stellar mass for three different over-density bins. The vertical dotted line shows the representativeness limit of our survey. We show the best fit (with errors) from Eq. 6 for each density bin as shaded regions. We find an underlying correlation between stellar masses and D_n4000 , with the median D_n4000 of galaxies in high-density regions being larger than what is found in low-density regions. The difference between low and high-density environments is larger at higher stellar masses. We compare with the results from GCLASS (Muzzin et al. 2012), from VVDS (Vergani et al. 2008), from SHARDS (Hernán-Caballero et al. 2013), and from LEGA-C (Wu et al. 2018) which also show the same trends. We also show here the median value of D_n4000 as a function of both stellar mass and local density on in the right panel. This map is a smooth interpolation of the trends found in our sample and highlights the increase of the median D_n4000 with increasing stellar mass and local density.

Table 1. Results of the linear fits $X = m \times \log_{10}(M_{\star}/10^{10}M_{\odot}) + b$ to $\text{EW}_{[\text{OII}]}$ and D_n4000 that are shown in Figs. 6 and 7. We note that the slope is fixed for the [OII] related fits, and the y-intercept is fixed for the D_n4000 related fits.

X	$\log_{10}(1 + \delta) < 0.1$		$0.1 < \log_{10}(1 + \delta) < 0.6$		$\log_{10}(1 + \delta) > 0.6$	
	m	b	m	b	m	b
$\text{EW}_{[\text{OII}]}$	[8.04]	-17 ± 1	[8.04]	-16 ± 1	[8.04]	-15 ± 2
D_n4000	0.14 ± 0.02	[1.15]	0.29 ± 0.03	[1.15]	0.37 ± 0.05	[1.15]

our estimated errors, we cannot pinpoint any dependence of the line strength with the environment. Concerning the absorption component of H δ , the results hint at a dependence on the environment that depends itself on the stellar mass we consider. However, only the rise from low to intermediate densities in absorption EW for higher stellar masses is of some significance (from $0.7^{+0.5}_{-0.7} \text{ \AA}$ to $1.8^{+0.3}_{-0.2} \text{ \AA}$). Interestingly, at intermediate densities, the H δ absorption line has a similar equivalent width at all stellar masses.

With respect to the emission component of H δ , we find a tentative trend of the emission being stronger for less massive galaxies (as reported for the full sample in Fig. 5). We find no significant dependence with local density for each of the stellar mass ranges considered.

4.2.4. Anti-correlation between D_n4000 and $\text{EW}_{[\text{OII}]}$

We show in Fig. 9 an anti-correlation between the strength of the 4000 \AA break (traced by D_n4000) and the [OII] line equivalent width which broadly traces the sSFR (Darvish et al. 2015a). The observed trend seems to be partially induced by a variation in stellar mass and we find that the most massive galaxies ($\log_{10}(M_{\star}/M_{\odot}) > 11$) in intermediate and high-density regions show an increase in D_n4000 while having similar [OII] line equivalent widths as lower density regions. We attempt at qualifying

the correlation by fitting two linear models on two different stellar mass regimes

$$Y = \begin{cases} (-3.9 \pm 0.7) \times X + (5.8 \pm 0.9) & \text{if } 10 < M < 11 \\ (-0.8 \pm 0.2) \times X + (1.9 \pm 0.3) & \text{if } M > 11 \end{cases} \quad (7)$$

with $Y = \log_{10}(-\text{EW}_{[\text{OII}]})$, $X = D_n4000$, and $M = \log_{10}(M_{\star}/M_{\odot})$. This means a steeper slope for the less massive galaxies when compared to the one for the most massive galaxies. We find that the departure from the lower stellar mass relation happens at lower stellar masses for higher density regions, with galaxies in field-like regions never departing from that relation.

This relation is qualitatively similar to what is reported for galaxies more massive than $10^{10}M_{\odot}$ in zCOSMOS at $0.48 < z < 1.2$ by Vergani et al. (2010), although they only use this relation to compare the selection of star-forming, quiescent, and post-starburst galaxies. We interpret this relation as a combination of two phenomena. At lower stellar masses ($< 10^{11}M_{\odot}$) it is likely a consequence of a declining sSFR with the stellar mass that drives the decrease of [OII] equivalent width and an increase of D_n4000 . At higher stellar masses there are possible other ionizing mechanisms than star formation alone. We note that the fraction of quiescent galaxies is higher at high stellar masses and also higher in the high-density regions we probe PA18. It is

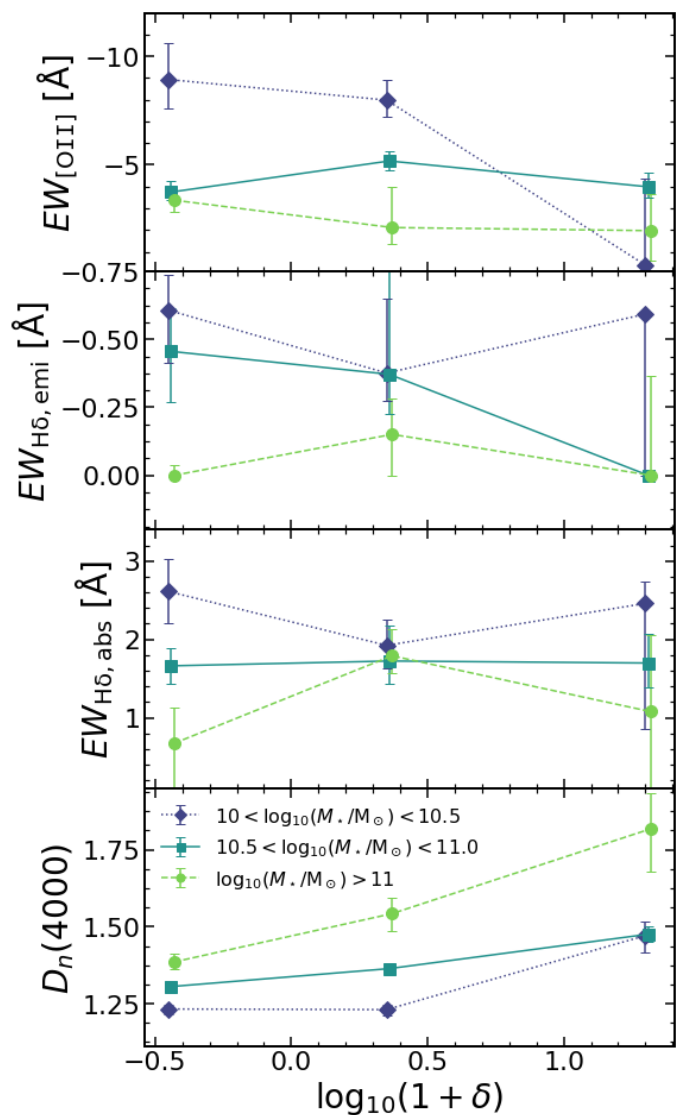


Fig. 8. The dependence of the three spectral indices detailed in Section 3.2 (from top to bottom - [OII] equivalent width, H δ equivalent width, and D_n4000) as a function of over-density in three stellar mass bins. This highlights the impact of both stellar mass and environment on the observed spectral properties of galaxies.

also found in the literature that for such red systems, the [OII] line is likely dominated by AGN/LINER powered emission (e.g. Yan et al. 2006; Lemaux et al. 2010). More recently, resolved studies of galaxies have also revealed that LINER-like emission can be widespread and is thought to be powered by an extended population of post-Asymptotic Red Giant branch stars (see e.g. Singh et al. 2013; Gomes et al. 2016; Belfiore et al. 2016, 2017). It is also possible that an increased stellar metallicity would result in an increase of D_n4000 at fixed $EW_{[OII]}$, but there is little evidence that metallicity strongly depends on environment (e.g. for gas-phase metallicity Ellison et al. 2009; Cooper et al. 2008; Darvish et al. 2015a; Sobral et al. 2015, 2016; Wu et al. 2017 and for stellar metallicity Harrison et al. 2011). Another likely explanation is that there is an underlying older stellar population in higher density environments (as hinted from Section 4.2.2) with residual star formation producing the observed [O II] emission. This could be seen through a similar break in the sSFR- D_n4000 relation, which we do not observe as prominently in our sample. However, we cannot test on the possible LINER-

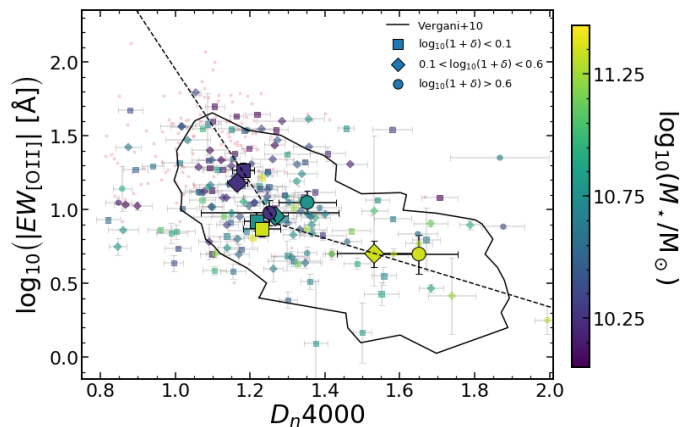


Fig. 9. The observed relation between D_n4000 and $\log_{10}(-EW_{[OII]})$ for individual galaxies (small symbols) and median per stellar mass bin (large symbols), colour coded by their stellar mass. The small purple dots show the values for galaxies with $\log_{10}(M_{\star}/M_{\odot}) < 10$. Different symbols correspond to different over-densities. The dashed lines are linear fits to the data of individual galaxies in two stellar mass subsamples (see text for details): the steeper slope is the fit for galaxies with $10 < \log_{10}(M_{\star}/M_{\odot}) < 11$; the shallower slope is the fit for galaxies with $\log_{10}(M_{\star}/M_{\odot}) > 11$. This highlights the underlying anti-correlation between the observed strength of the [OII] emission and the strength of the 4000Å break. We show as a black contour the location of 85% of the zCOSMOS sample at $0.48 < z < 1.2$ and with stellar masses greater than $10^{10}M_{\odot}$ (Vergani et al. 2010).

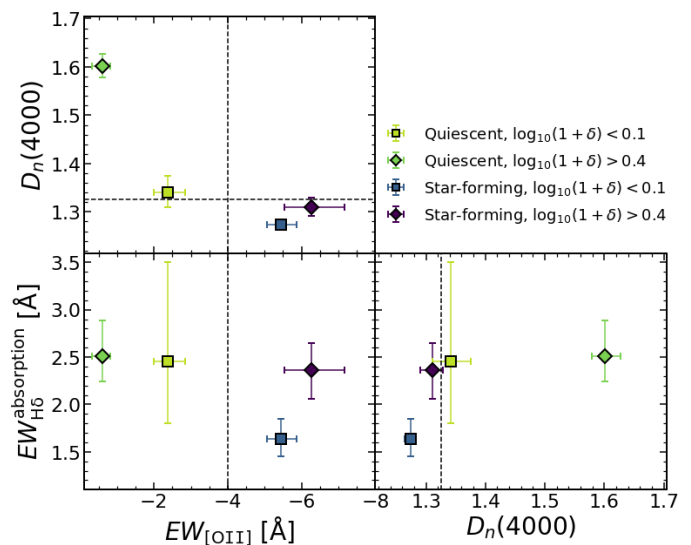


Fig. 10. We show the properties of composite spectra of quiescent and star-forming galaxies selected through their sSFR (separation at $\log_{10}(sSFR) = -11$, see also PA18) in low- (diamonds) and high-density regions (squares). The dotted lines are for $D_n4000 = 1.325$ and $EW_{[OII]} = 4 \text{ \AA}$ and shown to guide the eye. We see that these two populations are separated in D_n4000 and $EW_{[OII]}$ and that we can also find some environmental effects within each population of galaxies. We find that it is in high-density regions that the quiescent and star-forming populations are more clearly separated.

like emission nature of [OII] without spectroscopic observations at longer wavelengths.

4.3. Star formation activity in different environments

Finally, we have also studied the composite spectra of quiescent and star-forming galaxies (more massive than $10^{10}M_\odot$ separated at SED-derived $\log_{10}(sSFR) = -11$, see PA18) in low ($\log_{10}(1 + \delta) < 0.1$) and high ($\log_{10}(1 + \delta) > 0.4$) density environments and summarize our results in Fig. 10 (see also Table A.1). We find that the two populations are separated with D_n4000 and $EW_{[OII]}$, as expected. Overall, we also find that the difference is larger in high-density regions.

When focusing on H δ absorption strength, we see stronger absorption in star-forming galaxies in high-density regions than at lower densities. These results are indicative of star-forming galaxies in high-density regions having undergone a recent burst of star formation (or being a mix of normal star-forming galaxies with a post-starburst population), or having dustier star-forming regions (e.g. Smail et al. 1999). That scenario would explain similar observed [OII] equivalent widths but a $\sim 50 \pm 20\%$ increase in the H δ absorption strength and only a small $\sim 3 \pm 2\%$ increase in D_n4000 (see e.g. Balogh et al. 1999; Poggianti et al. 1999; Mansheim et al. 2017b). For field star-forming galaxies we find lower equivalent widths for the H δ absorption. This may hint at a less bursty star-formation on these systems.

From estimates using a single stellar population model with a stellar mass-based stellar metallicity (see Section 3.3) we find that quenched galaxies in the densest regions are much older (assuming a SSP, $\sim 2.2^{+0.1}_{-0.4}$ Gyr) than those in the field ($\sim 0.54^{+0.09}_{-0.07}$ Gyr). These differences among quiescent galaxies with the environment are not found by Muzzin et al. (2012) or Mosleh et al. (2018). We note that both quiescent samples in low- and high-density regions have similar stellar mass distributions, so we should not expect this to be a simple consequence of an underlying mass-metallicity relation. We discuss further interpretations of our results in Section 5.2.

5. Discussion

Our results highlight that both stellar mass and environment play a role in the star formation history of galaxies. (as also reported by e.g. Iovino et al. 2010; Cucciati et al. 2010; Peng et al. 2010b; Li et al. 2011; Davidzon et al. 2016; Darvish et al. 2016; Kawinwanichakij et al. 2017). We see in Fig. 8 that stellar-mass influences the strength of the [OII] in all environments, showing weaker emission for the most massive galaxies, with stellar mass being the main driver of the observed changes. However, we see that the difference between populations of different stellar masses is affected by the environment. A similar result is also seen in H δ absorption, with field-like regions being the place where most differences are found. This is also seen clearly in D_n4000 where the difference among galaxies with different stellar masses depends on the local density, with galaxies in the field being the most similar.

5.1. Environmental effects on star formation

Figure 8 shows that for galaxies with stellar masses $10.5 < \log_{10}(M_\star/M_\odot) < 11$ there is a small increase (at $\sim 1.7\sigma$ level) in the observed emission strength of [OII] at filament-like densities when compared to field and cluster regions (see also Fig. 5 for stacks with all galaxies more massive than $10^{10}M_\odot$). Despite this trend hinting to a slightly higher sSFR at intermediate densities, it is not evidenced enough of any environmental impact on SFR at these stellar masses.

Considering the sample at $10.0 < \log_{10}(M_\star/M_\odot) < 10.5$ we find an overall decrease in the $EW_{[OII]}$ with increasing density, which is also seen for similar stellar masses in Tomczak et al. (2019). On the high stellar mass end of our sample, we see no effect of the environment on the observed $EW_{[OII]}$. This overall effect on the median sSFR can be linked to the results on the quenched fraction (f_Q) shown in PA18, where we find that at high stellar masses ($>10^{11}M_\odot$) there is no dependence effect on f_Q while at lower stellar masses there is an increase from intermediate- to high-density regions (see also e.g. Lemaux et al. 2018). Naturally, an increase of the quenched fraction (from $\sim 10\%$ to $\sim 50\%$ of the sample from low and intermediate to high-density regions, see Table A.1) results in a lower median sSFR value for the population. Both these results point to an environmental dependence of star formation at $10.0 < \log_{10}(M_\star/M_\odot) < 10.5$ (see also e.g. Peng et al. 2010a), while for more massive galaxies we see no major effect. This would support a scenario in which mass quenching mechanisms act to suppress star formation at high stellar masses, and local environment has a negligible impact on star formation (e.g. Peng et al. 2010a, 2012), but more recent studies see a different picture for massive galaxies in dense environments (e.g. Darvish et al. 2016).

A scenario that can explain these results must account for enhancement of star formation activity at intermediate densities and then some quenching mechanism that acts as galaxies move towards higher densities (which may be connected). This can be thought of as filaments being regions of higher probabilities for gas-rich galaxies to interact (e.g. Moss 2006; Perez et al. 2009; Li et al. 2009; Tonnesen & Cen 2012; Darvish et al. 2014; Malavasi et al. 2017) promoting compression of gas clouds and a peak in the SFR of the galaxy (e.g. Mihos & Hernquist 1996; Kewley et al. 2006; Ellison et al. 2008; Gallazzi et al. 2009a; Bekki 2009; Owers et al. 2012; Roediger et al. 2014). Since we are looking at a superstructure composed of several sub-clusters, it is also possible that activity related to cluster-cluster interactions are capable of enhancing star formation as well (e.g. Stroe et al. 2014, 2015; Sobral et al. 2015), although this might not always be the case (see e.g. Mansheim et al. 2017a).

5.2. Older population prevalence influenced by the environment

While we find in Fig. 5 that D_n4000 strongly correlates with stellar mass, we show in Fig. 8 that the strength of such correlation is strongly dependent on the environment. The fact that cluster galaxies have on average stronger 4000 Å breaks were already reported in other studies (see e.g. Muzzin et al. 2012), but we extend to a range of densities that is complementary to the sample of Muzzin et al. (2012), targeting rich clusters and the galaxies around them.

To explain the observed trend, we need that the time passed since the last relevant episode of star formation be different at each environment (see also e.g. Rettura et al. 2010, 2011; Darvish et al. 2016). When looking at the most massive galaxies ($\log_{10}(M_\star/M_\odot) > 11$) we find that they have older stellar populations in high-density regions when compared to the lower density region counterparts (5^{+3}_{-2} Gyr compared to $0.64^{+0.06}_{-0.07}$ Gyr at lower densities⁴). PA18 showed that, at these stellar masses, the quenched fraction is not changing with the environment, so it is not simply a larger fraction of red galaxies that can reproduce

⁴ We note that this age estimate is based on an SSP with a median stellar metallicity derived for individual subsamples, see Section 3.3.

the age differences. This would then require that massive galaxies in the high-density regions have become passive earlier than their field counterparts, which can be a consequence of denser regions having collapsed first and thus galaxies in such regions formed at earlier times (e.g. Thomas et al. 2005; Nelan et al. 2005). It is also consistent with the observed age difference for quenched galaxies in the field and cluster-like densities ($\sim 0.54^{+0.09}_{-0.07}$ Gyr and $\sim 2.2^{+0.1}_{-0.4}$ Gyr, respectively).

The lack of recent star formation in higher density regions can be linked to the gas accretion being lower in dense regions (e.g. van de Voort et al. 2017). Due to the prevalence of gas stripping in dense regions (e.g. Bahé et al. 2013; Jaffé et al. 2015; Poggianti et al. 2016), also seen in the lack of gas-rich galaxies in clusters (e.g. Boselli et al. 2016), there is little fuel to new star-forming episodes for massive galaxies. In lower-density environments (fields, filaments, or groups) it is more likely that gas can funnel to the massive galaxies from minor mergers or tidal interactions with gas-rich satellites (Poggianti et al. 2016). This is also consistent with the pre-processing of galaxies in filaments and groups (gas loss and quiescence) before in-fall in the cluster regions (Wetzel et al. 2013; Haines et al. 2015). The ram pressure from the denser regions can also act as an enhancement of star formation prior to quenching (see Section 5.1 and e.g. Poggianti et al. 2016). Thus, massive galaxies in high-density regions should grow through mergers of gas-poor galaxies (dry mergers, see e.g. Khochfar & Burkert 2003; Khochfar & Silk 2009; McIntosh et al. 2008; Lin et al. 2010; Davidzon et al. 2016; Martin et al. 2017) in order to build up their mass while maintaining an older stellar population. In this scenario, the dependence of the D_n4000 -stellar mass on the environment is explained by the fraction of gas-rich galaxies that are available for merging at each density, being less common at higher densities (e.g. Boselli et al. 2016). This is also in agreement to numerous reported trends of the quenched fraction (equivalent to the number of gas-poor galaxies) with environment (Peng et al. 2010b; Cucciati et al. 2010; Sobral et al. 2011; Muzzin et al. 2012; Darvish et al. 2016; PA18).

As we move to stellar masses $10 < \log_{10}(M_*/M_\odot) < 11$, the impact of environment is less pronounced (differences in D_n4000 between low- and high-density environments is smaller), although we still see slightly older stellar populations in higher density environments (~ 0.6 Gyr older than in low-density environments). In this case, we would require either that galaxies are still forming new stars or that if they are quenched, it happened more recently. Since we observe a rise of the quenched fraction with local density for these stellar masses in PA18, we would favour the latter scenario.

We can reconcile the environmental effects seen at high stellar masses in D_n4000 with those seen only at lower stellar masses in $EW[\text{OII}]$ and f_Q discussed in Section 5.1. The values of $EW[\text{OII}]$ and f_Q (directly related to a galaxy's sSFR by our definition) are probing star formation timescales of 10-100 Myr (e.g. Couch & Sharples 1987; Salim et al. 2007; da Cunha et al. 2008), while the value for D_n4000 can probe the lack of recent star formation on longer timescales (typically a few Gyr, see Section 3.3). These different tracers can then be thought of a difference between a galaxy being quenched or not (*instantaneous* star formation traced by $[\text{OII}]$) and the time that has passed since that quenching happened (traced by D_n4000). A simple explanation is possibly linked to the formation epoch of massive galaxies in different environments (e.g. Thomas et al. 2005; Nelan et al. 2005). Galaxies in cluster cores are formed earlier (due to earlier collapse of overdense regions) and therefore become passive earlier (having low

sSFR and high D_n4000 due to the median stellar age passively evolving because of the absence of further episodes of star formation) while galaxies in lower density regions can be recently quenched (having low sSFR and relatively low D_n4000) since their regions have collapsed later in cosmic time. It is also possible that faster quenching in high-density regions (e.g. Foltz et al. 2018; Socolovsky et al. 2018) could mimic the observations if galaxies formed at similar cosmic times. These scenarios would explain the higher values of D_n4000 and lower values of $H\delta$ absorption equivalent width for high-density quiescent galaxies when compared to the lower density counterparts. Both scenarios require that higher density environments ultimately suppress or do not allow for new star formation episodes in galaxies (which might happen through bursts or in a continuous decline).

We note that a higher metallicity in high-density regions (not encoded in our assumed stellar mass-metallicity relation in Section 3.3, e.g. Sobral et al. 2015) could mitigate some of the observed differences in our age estimates. If we consider a metallicity of $2.5Z_\odot$ (4.5 times higher than the expected value from the median stellar mass at this redshift), we would have an estimate of age ~ 1.7 Gyr for quiescent galaxies in high-density regions. However, other studies find only marginal differences in gas-phase metallicity between field and cluster quiescent galaxies (e.g. Ellison et al. 2009 see also e.g. Cooper et al. 2008; Darvish et al. 2015a; Sobral et al. 2016; Wu et al. 2017 for similar results on star-forming galaxies), also seen in stellar metallicity (e.g. Harrison et al. 2011), making it unlikely that a metallicity dependence on environment can explain the observed differences.

6. Conclusions

We have presented the spectroscopic properties of 466 galaxies in and around a $z \sim 0.84$ superstructure in the COSMOS field targeted with the VIS³COS survey (Paulino-Afonso et al. 2018). We explore the spectral properties of galaxies and relate those to their stellar mass and environment, by measuring and interpreting $[\text{OII}]$, $H\delta$, and D_n4000 . We use $[\text{OII}]$ equivalent width as a tracer of sSFR, $H\delta$ as a tracer of current episodes (from emission) or recent bursts (from absorption) of star formation, and D_n4000 as a tracer of the average age of the stellar population. We present results both on individual galaxies and on composite spectra to evaluate the relative importance of stellar mass and/or the environment in the build-up of stellar populations in galaxies. Our main results are:

- We find no significant dependence of $H\delta$ absorption or emission components on the environment. We find that both $H\delta$ absorption or emission decrease with increasing stellar mass.
- The $[\text{OII}]\lambda 3727$ absolute line equivalent width decreases by a factor of ~ 3 from $\sim 10^{10.25}M_\odot$ to $\sim 10^{11.25}M_\odot$. We observe this decrease in all environments which trend is mostly a consequence of the underlying main sequence of star-forming galaxies.
- We find D_n4000 to increase with an increasing stellar mass in all environments. For stellar masses $10.0 < \log_{10}(M_*/M_\odot) < 10.5$ we see an impact of environment on the average stellar age ($0.32^{+0.06}_{-0.05}$ Gyr to 1.1 ± 0.2 Gyr, from low- to high-density regions). For the most massive galaxies ($\log_{10}(M_*/M_\odot) > 11$) the difference is much larger ($0.64^{+0.06}_{-0.07}$ Gyr to 5^{+3}_{-2} Gyr⁵).

⁵ We note that this age estimate is based on a single SSP. See Section 5.2.

- There is an anti-correlation between $\log_{10}(-EW_{[\text{OII}]})$ and D_n4000 (also seen in e.g. Vergani et al. 2010) which is mostly a consequence of the underlying correlations of these quantities with stellar mass. We find that the most massive galaxies ($\log_{10}(M_*/M_\odot) > 11$) in intermediate and high-density regions have higher D_n4000 while showing similar $EW_{[\text{OII}]}$ to lower density regions. This may hint at a different ionizing mechanism in high stellar mass galaxies operating in denser environments or be a consequence of older stellar populations residing in such regions.
- We find an increase in the [OII] equivalent width at intermediate densities for intermediate stellar mass galaxies ($10.5 < \log_{10}(M_*/M_\odot) < 11$) which may point to episodes of enhanced star formation (more stars formed per stellar mass) on timescales around 10 Myr.

Based on our results on D_n4000 , we hypothesize that the most massive galaxies ($\log_{10}(M_*/M_\odot) > 11$) have ceased star formation earlier (by a few Gyr, depending on the stellar metallicity and assumed star formation history) in high-density environments than their field counterparts. Lower stellar mass galaxies ($10 < \log_{10}(M_*/M_\odot) < 11$) need to have quenched more recently at similar environments (or still have ongoing lower levels of star formation), since they have signs of younger stellar populations when compared to the most massive sample. The observed older stellar populations of massive galaxies in high-density environments point to a lack of recent episodes of significant star formation. This is compatible with a scenario where either all stars formed *in-situ* and earlier or that they likely growth mechanism through dry merging events. In lower-density environments, they are either continuously forming new stars (at lower rates) or experiencing merging events with gas-rich galaxies fuelling new episodes of star formation. Such a scenario is required to explain the dependence of D_n4000 on the environment at these stellar masses.

Acknowledgements. We thank the anonymous referee for the insightful and useful comments that helped improve the quality and readability of the paper. This work was supported by Fundação para a Ciência e a Tecnologia (FCT) through the research grant UID/FIS/04434/2013. APA, PhD::SPACE fellow, acknowledges support from the FCT through the fellowship PD/BD/52706/2014. DS acknowledges financial support from Lancaster University through an Early Career Internal Grant A100679. BD acknowledges financial support from NASA through the Astrophysics Data Analysis Program (ADAP), grant number NNX12AE20G, and the National Science Foundation, grant number 1716907. IRS acknowledges support from the ERC Advanced Grant DUSTYGAL (321334), STFC (ST/P000541/1) and a Royal Society/Wolfson Merit award. PNB is grateful for support from STFC (ST/M001229/1). This work was only possible by the use of the following PYTHON packages: NumPy & SciPy (Walt et al. 2011; Jones et al. 2001), Matplotlib (Hunter 2007), Astropy (Astropy Collaboration et al. 2013), and EzGal (Mancone & Gonzalez 2012).

References

Aragón-Calvo, M. A., van de Weygaert, R., & Jones, B. J. T. 2010, MNRAS, 408, 2163
 Astropy Collaboration, Robitaille, T. P., Tollerud, E. J., et al. 2013, A&A, 558, A33
 Bahé, Y. M., McCarthy, I. G., Balogh, M. L., & Font, A. S. 2013, MNRAS, 430, 3017
 Balogh, M. L., Morris, S. L., Yee, H. K. C., Carlberg, R. G., & Ellingson, E. 1999, ApJ, 527, 54
 Balogh, M. L., Navarro, J. F., & Morris, S. L. 2000, ApJ, 540, 113
 Bekki, K. 2009, MNRAS, 399, 2221
 Belfiore, F., Maiolino, R., Maraston, C., et al. 2017, MNRAS, 466, 2570
 Belfiore, F., Maiolino, R., Maraston, C., et al. 2016, MNRAS, 461, 3111
 Best, P. N. 2004, MNRAS, 351, 70
 Birnboim, Y. & Dekel, A. 2003, MNRAS, 345, 349
 Birnboim, Y., Dekel, A., & Neistein, E. 2007, MNRAS, 380, 339

Blanton, M. R., Eisenstein, D., Hogg, D. W., Schlegel, D. J., & Brinkmann, J. 2005, ApJ, 629, 143
 Boselli, A., Roehly, Y., Fossati, M., et al. 2016, A&A, 596, A11
 Bower, R. G., Benson, A. J., Malbon, R., et al. 2006, MNRAS, 370, 645
 Bridge, J. S., Gronwall, C., Ciardullo, R., et al. 2015, ApJ, 799, 205
 Bruzual, A. G. 1983, ApJ, 273, 105
 Bruzual, G. & Charlot, S. 2003, MNRAS, 344, 1000
 Calzetti, D., Armus, L., Bohlin, R. C., et al. 2000, ApJ, 533, 682
 Cava, A., Pérez-González, P. G., Eliche-Moral, M. C., et al. 2015, ApJ, 812, 155
 Chabrier, G. 2003, ApJ, 586, L133
 Charlot, S. & Fall, S. M. 2000, ApJ, 539, 718
 Cohen, S. A., Hickox, R. C., Wegner, G. A., Einasto, M., & Vennik, J. 2017, ApJ, 835, 56
 Combes, F., García-Burillo, S., Braine, J., et al. 2013, A&A, 550, A41
 Cooke, E. A., Smail, I., Stach, S. M., et al. 2019, MNRAS, 486, 3047
 Cooper, M. C., Tremonti, C. A., Newman, J. A., & Zabludoff, A. I. 2008, MNRAS, 390, 245
 Coppin, K. E. K., Geach, J. E., Webb, T. M. A., et al. 2012, ApJ, 749, L43
 Couch, W. J. & Sharples, R. M. 1987, MNRAS, 229, 423
 Cox, T. J., Jonsson, P., Primack, J. R., & Somerville, R. S. 2006, MNRAS, 373, 1013
 Croton, D. J., Springel, V., White, S. D. M., et al. 2006, MNRAS, 365, 11
 Cucciati, O., Iovino, A., Kovač, K., et al. 2010, A&A, 524, A2
 Cucciati, O., Iovino, A., Marinoni, C., et al. 2006, A&A, 458, 39
 da Cunha, E., Charlot, S., & Elbaz, D. 2008, MNRAS, 388, 1595
 Darvish, B., Martin, C., Gonçalves, T. S., et al. 2018, ApJ, 853, 155
 Darvish, B., Mobasher, B., Martin, D. C., et al. 2017, ApJ, 837, 16
 Darvish, B., Mobasher, B., Sobral, D., et al. 2015a, ApJ, 814, 84
 Darvish, B., Mobasher, B., Sobral, D., et al. 2016, ApJ, 825, 113
 Darvish, B., Mobasher, B., Sobral, D., Scoville, N., & Aragon-Calvo, M. 2015b, ApJ, 805, 121
 Darvish, B., Sobral, D., Mobasher, B., et al. 2014, ApJ, 796, 51
 Davidzon, I., Cucciati, O., Bolzonella, M., et al. 2016, A&A, 586, A23
 De Rossi, M. E., Bower, R. G., Font, A. S., Schaye, J., & Theuns, T. 2017, MNRAS, 472, 3354
 Dekel, A. & Cox, T. J. 2006, MNRAS, 370, 1445
 Dressler, A. 1980, ApJ, 236, 351
 Dressler, A., Oemler, Jr., A., Poggianti, B. M., et al. 2004, ApJ, 617, 867
 Efstathiou, G. 2000, MNRAS, 317, 697
 Elbaz, D., Daddi, E., Le Borgne, D., et al. 2007, A&A, 468, 33
 Ellison, S. L., Patton, D. R., Simard, L., & McConnachie, A. W. 2008, AJ, 135, 1877
 Ellison, S. L., Simard, L., Cowan, N. B., et al. 2009, MNRAS, 396, 1257
 Erfanianfar, G., Popesso, P., Finoguenov, A., et al. 2016, MNRAS, 455, 2839
 Fabian, A. C. 2012, ARA&A, 50, 455
 Finoguenov, A., Guzzo, L., Hasinger, G., et al. 2007, ApJS, 172, 182
 Foltz, R., Wilson, G., Muzzin, A., et al. 2018, ApJ, 866, 136
 Fritz, J., Poggianti, B. M., Cava, A., et al. 2014, A&A, 566, A32
 Fujita, Y. 1998, ApJ, 509, 587
 Gabor, J. M., Davé, R., Finlator, K., & Oppenheimer, B. D. 2010, MNRAS, 407, 749
 Gallazzi, A., Bell, E. F., Wolf, C., et al. 2009a, ApJ, 690, 1883
 Gallazzi, A., Bell, E. F., Wolf, C., et al. 2009b, ApJ, 690, 1883
 Gallazzi, A., Charlot, S., Brinchmann, J., White, S. D. M., & Tremonti, C. A. 2005, MNRAS, 362, 41
 Geach, J. E., Smail, I., Moran, S. M., Treu, T., & Ellis, R. S. 2009, ApJ, 691, 783
 Gomes, J. M., Papaderos, P., Vílchez, J. M., et al. 2016, A&A, 585, A92
 Gunn, J. E. & Gott, III, J. R. 1972, ApJ, 176, 1
 Haines, C. P., Pereira, M. J., Smith, G. P., et al. 2015, ApJ, 806, 101
 Harrison, C. D., Colless, M., Kuntschner, H., et al. 2011, MNRAS, 413, 1036
 Hernán-Caballero, A., Alonso-Herrero, A., Pérez-González, P. G., et al. 2013, MNRAS, 434, 2136
 Hunter, J. D. 2007, Computing In Science & Engineering, 9, 90
 Ideue, Y., Nagao, T., Taniguchi, Y., et al. 2009, ApJ, 700, 971
 Ilbert, O., Capak, P., Salvato, M., et al. 2009, ApJ, 690, 1236
 Ilbert, O., McCracken, H. J., Le Fèvre, O., et al. 2013, A&A, 556, A55
 Iovino, A., Cucciati, O., Scodreggio, M., et al. 2010, A&A, 509, A40
 Jaffé, Y. L., Smith, R., Candlish, G. N., et al. 2015, MNRAS, 448, 1715
 Jones, E., Oliphant, T., Peterson, P., et al. 2001, SciPy: Open source scientific tools for Python, [Online; accessed 2016-03-23]
 Kashino, D., Silverman, J. D., Rodighiero, G., et al. 2013, ApJ, 777, L8
 Kauffmann, G., Heckman, T. M., White, S. D. M., et al. 2003, MNRAS, 341, 33
 Kauffmann, G., White, S. D. M., Heckman, T. M., et al. 2004, MNRAS, 353, 713
 Kawinwanichakij, L., Papovich, C., Quadri, R. F., et al. 2017, ApJ, 847, 134
 Kennicutt, R. C. & Evans, N. J. 2012, ARA&A, 50, 531
 Kennicutt, Jr., R. C. 1998, ARA&A, 36, 189
 Kereš, D., Katz, N., Davé, R., Fardal, M., & Weinberg, D. H. 2009a, MNRAS, 396, 2332
 Kereš, D., Katz, N., Fardal, M., Davé, R., & Weinberg, D. H. 2009b, MNRAS, 395, 160

- Kereš, D., Katz, N., Weinberg, D. H., & Davé, R. 2005, *MNRAS*, 363, 2
- Kewley, L. J., Geller, M. J., & Barton, E. J. 2006, *AJ*, 131, 2004
- Kewley, L. J., Geller, M. J., & Jansen, R. A. 2004, *AJ*, 127, 2002
- Khochfar, S. & Burkert, A. 2003, *ApJ*, 597, L117
- Khochfar, S. & Silk, J. 2009, *MNRAS*, 397, 506
- Kocevski, D. D., Lemaux, B. C., Lubin, L. M., et al. 2011, *ApJ*, 737, L38
- Kodama, T., Balogh, M. L., Smail, I., Bower, R. G., & Nakata, F. 2004, *MNRAS*, 354, 1103
- Kodama, T., Smail, I., Nakata, F., Okamura, S., & Bower, R. G. 2001, *ApJ*, 562, L9
- Kormendy, J. 2013, *Secular Evolution in Disk Galaxies*, ed. J. Falcón-Barroso & J. H. Knapen, 1
- Koyama, Y., Kodama, T., Shimasaku, K., et al. 2010, *MNRAS*, 403, 1611
- Koyama, Y., Kodama, T., Shimasaku, K., et al. 2008, *MNRAS*, 391, 1758
- Koyama, Y., Smail, I., Kurk, J., et al. 2013, *MNRAS*, 434, 423
- Laigle, C., McCracken, H. J., Ilbert, O., et al. 2016, *ApJS*, 224, 24
- Larson, R. B., Tinsley, B. M., & Caldwell, C. N. 1980, *ApJ*, 237, 692
- Leethochawalit, N., Kirby, E. N., Moran, S. M., Ellis, R. S., & Treu, T. 2018, *ApJ*, 856, 15
- Lehnert, M. D., Le Tiran, L., Nesvadba, N. P. H., et al. 2013, *A&A*, 555, A72
- Lemaux, B. C., Lubin, L. M., Shapley, A., et al. 2010, *ApJ*, 716, 970
- Lemaux, B. C., Tomczak, A. R., Lubin, L. M., et al. 2018, *arXiv e-prints*, arXiv:1812.04624
- Lewis, I., Balogh, M., De Propris, R., et al. 2002, *MNRAS*, 334, 673
- Li, C., Kauffmann, G., Jing, Y. P., et al. 2006, *MNRAS*, 368, 21
- Li, I. H., Glazebrook, K., Gilbank, D., et al. 2011, *MNRAS*, 411, 1869
- Li, I. H., Yee, H. K. C., & Ellingson, E. 2009, *ApJ*, 698, 83
- Lin, L., Cooper, M. C., Jian, H.-Y., et al. 2010, *ApJ*, 718, 1158
- Ma, X., Hopkins, P. F., Faucher-Giguère, C.-A., et al. 2016, *MNRAS*, 456, 2140
- Madau, P. & Dickinson, M. 2014, *ARA&A*, 52, 415
- Malavasi, N., Arnouts, S., Vibert, D., et al. 2017, *MNRAS*, 465, 3817
- Mancone, C. L. & Gonzalez, A. H. 2012, *Publications of the Astronomical Society of the Pacific*, 124, 606
- Mansheim, A. S., Lemaux, B. C., Dawson, W. A., et al. 2017a, *ApJ*, 834, 205
- Mansheim, A. S., Lemaux, B. C., Tomczak, A. R., et al. 2017b, *MNRAS*, 469, L20
- Martin, D. C., Gonçalves, T. S., Darvish, B., Seibert, M., & Schiminovich, D. 2017, *ApJ*, 842, 20
- Masters, D. & Capak, P. 2011, *PASP*, 123, 638
- McIntosh, D. H., Guo, Y., Hertzberg, J., et al. 2008, *MNRAS*, 388, 1537
- Merritt, D. 1984, *ApJ*, 276, 26
- Mihos, J. C. & Hernquist, L. 1996, *ApJ*, 464, 641
- Moore, B., Lake, G., & Katz, N. 1998, *ApJ*, 495, 139
- Mosleh, M., Tavasoli, S., & Tacchella, S. 2018, *ApJ*, 861, 101
- Moss, C. 2006, *MNRAS*, 373, 167
- Muzzin, A., Wilson, G., Yee, H. K. C., et al. 2012, *ApJ*, 746, 188
- Nantais, J. B., Rettura, A., Lidman, C., et al. 2013, *A&A*, 556, A112
- Nelan, J. E., Smith, R. J., Hudson, M. J., et al. 2005, *ApJ*, 632, 137
- Oemler, Jr., A. 1974, *ApJ*, 194, 1
- Oemler, Jr., A., Dressler, A., Kelson, D., et al. 2009, *ApJ*, 693, 152
- Oke, J. B. & Gunn, J. E. 1983, *ApJ*, 266, 713
- Owers, M. S., Couch, W. J., Nulsen, P. E. J., & Randall, S. W. 2012, *ApJ*, 750, L23
- Pannella, M., Elbaz, D., Daddi, E., et al. 2015, *ApJ*, 807, 141
- Patel, S. G., Holden, B. P., Kelson, D. D., Illingworth, G. D., & Franx, M. 2009, *ApJ*, 705, L67
- Paulino-Afonso, A., Sobral, D., Darvish, B., et al. 2018, *A&A*, 620, A186
- Peng, C. Y., Ho, L. C., Impey, C. D., & Rix, H.-W. 2010a, *AJ*, 139, 2097
- Peng, Y.-j., Lilly, S. J., Kovač, K., et al. 2010b, *ApJ*, 721, 193
- Peng, Y.-j., Lilly, S. J., Renzini, A., & Carollo, M. 2012, *ApJ*, 757, 4
- Perez, J., Tissera, P., Padilla, N., Alonso, M. S., & Lambas, D. G. 2009, *MNRAS*, 399, 1157
- Poggianti, B. M., Aragón-Salamanca, A., Zaritsky, D., et al. 2009, *ApJ*, 693, 112
- Poggianti, B. M. & Barbaro, G. 1997, *A&A*, 325, 1025
- Poggianti, B. M., Fasano, G., Omizzolo, A., et al. 2016, *AJ*, 151, 78
- Poggianti, B. M., Smail, I., Dressler, A., et al. 1999, *ApJ*, 518, 576
- Poggianti, B. M., von der Linden, A., De Lucia, G., et al. 2006, *ApJ*, 642, 188
- Popesso, P., Rodighiero, G., Saintonge, A., et al. 2011, *A&A*, 532, A145
- Puchwein, E. & Springel, V. 2013, *MNRAS*, 428, 2966
- Rettura, A., Mei, S., Stanford, S. A., et al. 2011, *ApJ*, 732, 94
- Rettura, A., Rosati, P., Nonino, M., et al. 2010, *ApJ*, 709, 512
- Roediger, E., Brügggen, M., Owers, M. S., Ebeling, H., & Sun, M. 2014, *MNRAS*, 443, L114
- Salim, S., Rich, R. M., Charlot, S., et al. 2007, *ApJS*, 173, 267
- Santos, J. S., Altieri, B., Popesso, P., et al. 2013, *MNRAS*, 433, 1287
- Santos, J. S., Altieri, B., Tanaka, M., et al. 2014, *MNRAS*, 438, 2565
- Savaglio, S., Glazebrook, K., Le Borgne, D., et al. 2005, *ApJ*, 635, 260
- Scoville, N., Abraham, R. G., Aussel, H., et al. 2007, *ApJS*, 172, 38
- Scoville, N., Arnouts, S., Aussel, H., et al. 2013, *ApJS*, 206, 3
- Singh, R., van de Ven, G., Jahnke, K., et al. 2013, *A&A*, 558, A43
- Siudek, M., Małek, K., Scodreggio, M., et al. 2017, *A&A*, 597, A107
- Smail, I., Morrison, G., Gray, M. E., et al. 1999, *ApJ*, 525, 609
- Sobral, D., Best, P. N., Smail, I., et al. 2011, *MNRAS*, 411, 675
- Sobral, D., Best, P. N., Smail, I., et al. 2014, *MNRAS*, 437, 3516
- Sobral, D., Stroe, A., Dawson, W. A., et al. 2015, *MNRAS*, 450, 630
- Sobral, D., Stroe, A., Koyama, Y., et al. 2016, *MNRAS*, 458, 3443
- Socolovsky, M., Almaini, O., Hatch, N. A., et al. 2018, *MNRAS*, 476, 1242
- Somerville, R. S., Hopkins, P. F., Cox, T. J., Robertson, B. E., & Hernquist, L. 2008, *MNRAS*, 391, 481
- Stach, S. M., Swinbank, A. M., Smail, I., et al. 2017, *ApJ*, 849, 154
- Stroe, A., Sobral, D., Dawson, W., et al. 2015, *MNRAS*, 450, 646
- Stroe, A., Sobral, D., Paulino-Afonso, A., et al. 2017, *MNRAS*, 465, 2916
- Stroe, A., Sobral, D., Röttgering, H. J. A., & van Weeren, R. J. 2014, *MNRAS*, 438, 1377
- Thomas, D., Maraston, C., Bender, R., & Mendes de Oliveira, C. 2005, *ApJ*, 621, 673
- Tomczak, A. R., Lemaux, B. C., Lubin, L. M., et al. 2019, *MNRAS*, 484, 4695
- Tonnesen, S. & Cen, R. 2012, *MNRAS*, 425, 2313
- Tran, K.-V. H., Papovich, C., Saintonge, A., et al. 2010, *ApJ*, 719, L126
- Tremonti, C. A., Heckman, T. M., Kauffmann, G., et al. 2004, *ApJ*, 613, 898
- van de Voort, F., Bahé, Y. M., Bower, R. G., et al. 2017, *MNRAS*, 466, 3460
- van der Burg, R. F. J., Muzzin, A., Hoekstra, H., et al. 2013, *A&A*, 557, A15
- Vergani, D., Scodreggio, M., Pozzetti, L., et al. 2008, *A&A*, 487, 89
- Vergani, D., Zamorani, G., Lilly, S., et al. 2010, *A&A*, 509, A42
- Walt, S. v. d., Colbert, S. C., & Varoquaux, G. 2011, *Computing in Science & Engineering*, 13, 22
- Wetzell, A. R., Tinker, J. L., Conroy, C., & van den Bosch, F. C. 2013, *MNRAS*, 432, 336
- Whitaker, K. E., van Dokkum, P. G., Brammer, G., & Franx, M. 2012, *ApJ*, 754, L29
- Wild, V., Charlot, S., Brinchmann, J., et al. 2011, *MNRAS*, 417, 1760
- Worthey, G. & Ottaviani, D. L. 1997, *ApJS*, 111, 377
- Wu, P.-F., van der Wel, A., Gallazzi, A., et al. 2018, *ApJ*, 855, 85
- Wu, P.-F., Zahid, H. J., Hwang, H. S., & Geller, M. J. 2017, *MNRAS*, 468, 1881
- Wuyts, S., Förster Schreiber, N. M., Lutz, D., et al. 2011, *ApJ*, 738, 106
- Yan, R., Newman, J. A., Faber, S. M., et al. 2006, *ApJ*, 648, 281
- Zahid, H. J., Geller, M. J., Kewley, L. J., et al. 2013, *ApJ*, 771, L19
- Zahid, H. J., Kewley, L. J., & Bresolin, F. 2011, *ApJ*, 730, 137

Appendix A: Detailed spectral stack results

In this section, we briefly describe some of the observed features in the composite spectra and refer any quantitative analysis to Section 3.2.

We show in Fig. A.1 the composite spectra in bins of stellar mass. We observe a strong decrease in [OII] line flux from low to high stellar masses. We also see the relative strength of the two doublet lines changing with stellar mass (a quantitative analysis on the electron density estimates will be subject of a future paper). We find a decrease of the emission strength of Balmer lines (H γ , H δ , H ϵ , H ζ , H θ) with increasing stellar mass. At the same time, the prominence of the absorption features is increasingly noticeable at higher stellar masses. We also note the presence of [NIII] emission in some spectra which will be the subject of a forthcoming paper based on the VIS³COS survey.

In Fig.A.2 we show our findings of the stacked spectra in bins of over-density. In terms of the [OII] emission, we find a decreasing line strength from low to high-density regions (see also PA18). In terms of the H δ line, we also see a dependence on local density. We find an increase in the absorption strength from low- to high-density and a decrease of the emission component.

Finally, in Fig. A.3 we show the composite spectra binned by SFR. As expected, the [OII] emission is stronger for high SFR galaxies. In terms of their H δ absorption, we see a stronger absorption in higher SFR galaxies.

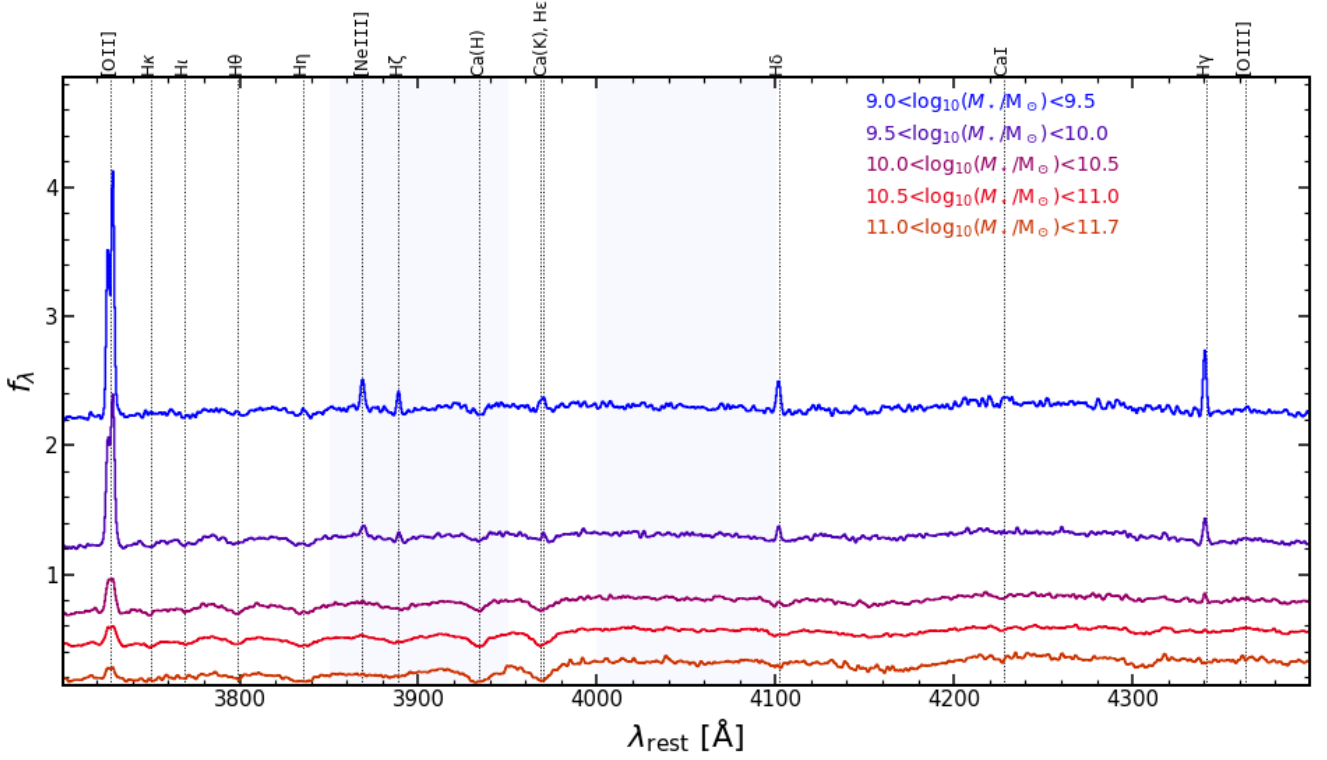


Fig. A.1. Resulting median composite spectra normalized at 4150-4300 Å and associated error (solid line + shaded region) in bins of stellar mass (low to high stellar mass from top to bottom). We apply a vertical offset for visualization purposes. We highlight with vertical lines the strongest features that we see on our spectra. The light grey vertical stripes show the spectral ranges which are used to compute D_n4000 .

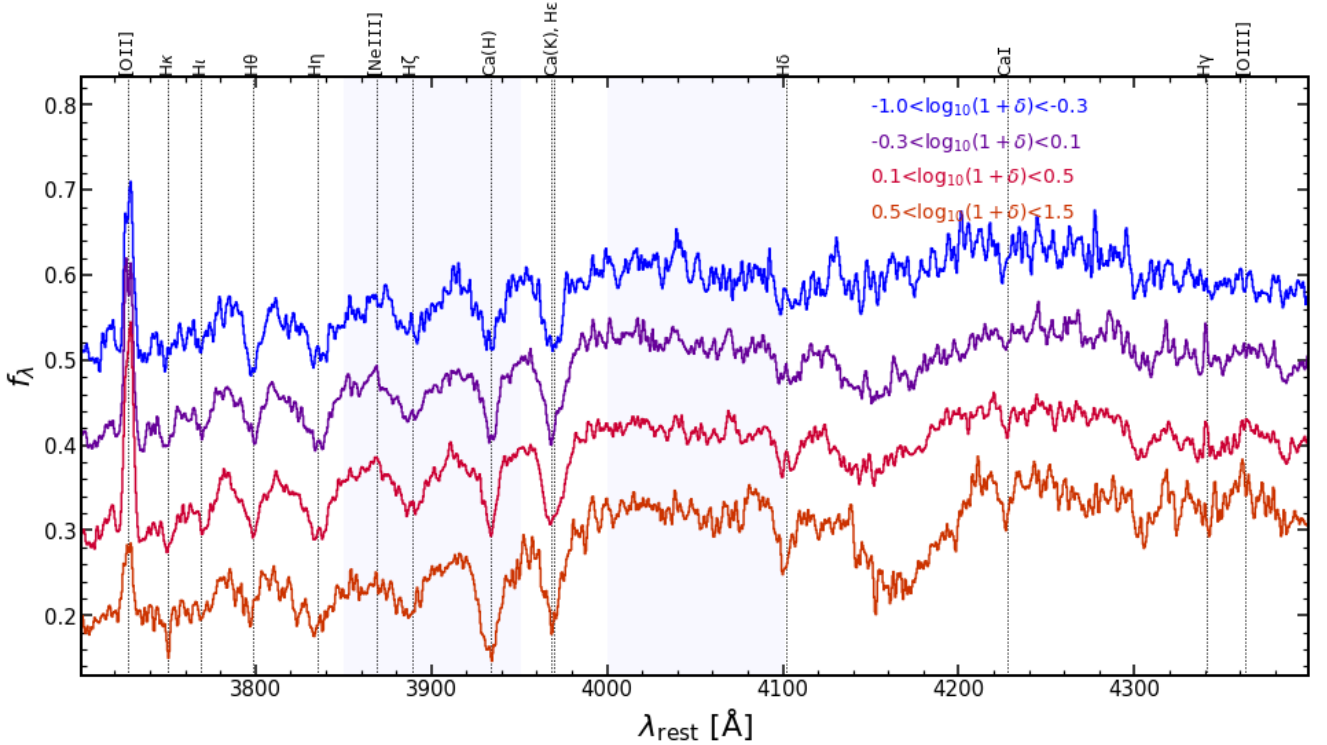


Fig. A.2. Resulting median composite spectra stacks normalized at 4150-4300 Å and associated error (solid line + shaded region) in bins of local over-density (low- to high-density regions from top to bottom) for galaxies with stellar masses greater than $10^{10}M_{\odot}$. We apply a vertical offset for visualization purposes. We highlight with vertical lines the strongest features that we see on our spectra. The light grey vertical stripes show the spectral ranges which are used to compute D_n4000 .

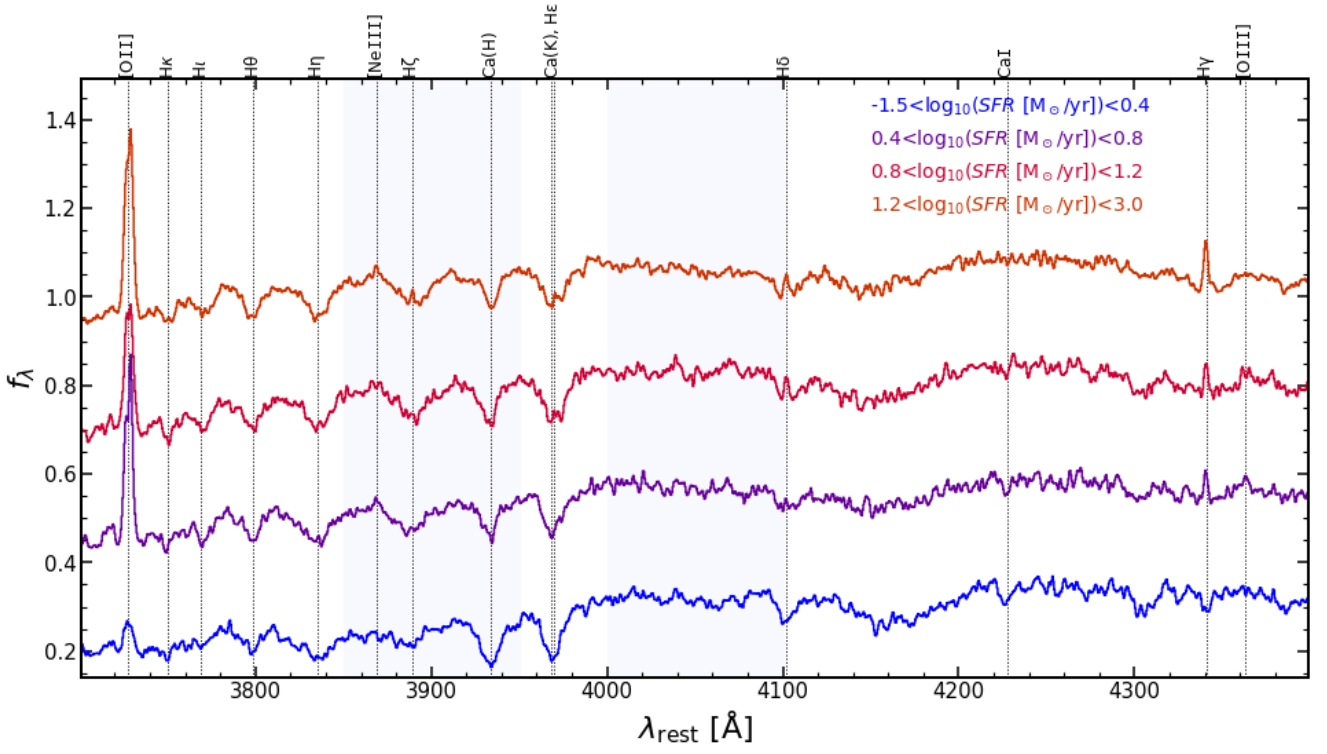


Fig. A.3. Resulting median composite spectra normalized at 4150–4300 Å and associated error (solid line + shaded region) in bins of star formation rate (high to low SFR from top to bottom) for galaxies with stellar masses greater than $10^{10}M_{\odot}$. We apply a vertical offset for visualization purposes. We highlight with vertical lines the strongest features that we see on our spectra. The light grey vertical stripes show the spectral ranges which are used to compute D_n4000 .

Table A.1. Summary table with the results for all spectroscopic indices in composite spectra shown in this paper. If only one variable is defined, it means that there is only a single selection for that row. Samples not selected in stellar mass in variables 1 and/or 2 have a minimum stellar-mass limit of $10^{10}M_{\odot}$. The third column shows the number of galaxies for each selection and the fourth column, the number of star-forming galaxies ($\log_{10}(sSFR) > -11$). The last column shows the stellar age for a single stellar population from Bruzual & Charlot (2003) derived as explained in Section 3.3. We opt not to show errors for the derived ages since the systematics due to our choice of metallicity and star formation history are much larger than those derived from observational errors on D_n4000 .

Variable 1	Variable 2	N_{all}	N_{SF}	[OII] Å	H δ_{emi} Å	H δ_{abs} Å	D_n4000	t_{SSP} Gyr
$9.0 \leq \log_{10}(M/M_{\odot}) < 9.5$	-	49	49	-27 ± 2	-2.5 ± 0.3	N/A	1.09 ± 0.01	$0.04^{+0.03}_{-0.01}$
$9.5 \leq \log_{10}(M/M_{\odot}) < 10.0$	-	111	108	-22 ± 2	$-1.01^{+0.09}_{-0.10}$	$3.8^{+0.6}_{-0.7}$	1.117 ± 0.009	0.06 ± 0.02
$10.0 \leq \log_{10}(M/M_{\odot}) < 10.5$	-	107	95	$-6.7^{+0.7}_{-0.8}$	$-0.6^{+0.3}_{-0.2}$	2.7 ± 0.2	$1.27^{+0.01}_{-0.02}$	$0.42^{+0.03}_{-0.04}$
$10.5 \leq \log_{10}(M/M_{\odot}) < 11.0$	-	148	121	-4.3 ± 0.3	$-0.39^{+0.07}_{-0.08}$	1.9 ± 0.2	1.365 ± 0.010	0.61 ± 0.03
$11.0 \leq \log_{10}(M/M_{\odot}) < 11.7$	-	40	19	$-2.0^{+0.3}_{-0.4}$	-0.1 ± 0.1	$1.1^{+0.3}_{-0.2}$	1.56 ± 0.03	$1.3^{+0.4}_{-0.2}$
$-1.0 \leq \log_{10}(1 + \delta) < -0.3$	-	42	32	$-4.0^{+0.6}_{-0.5}$	-0.4 ± 0.2	$2.3^{+0.7}_{-0.5}$	1.26 ± 0.02	0.35 ± 0.04
$-0.3 \leq \log_{10}(1 + \delta) < 0.1$	-	91	78	$-5.3^{+0.5}_{-0.6}$	$-0.3^{+0.1}_{-0.2}$	1.6 ± 0.2	1.31 ± 0.01	0.46 ± 0.03
$0.1 \leq \log_{10}(1 + \delta) < 0.5$	-	101	89	$-6.5^{+0.5}_{-0.4}$	$-0.5^{+0.1}_{-0.2}$	2.1 ± 0.2	1.31 ± 0.01	0.47 ± 0.03
$0.5 \leq \log_{10}(1 + \delta) < 1.5$	-	61	36	$-2.7^{+0.3}_{-0.5}$	$0.0^{+0.1}_{-0.4}$	$2.2^{+0.4}_{-0.3}$	1.51 ± 0.02	1.1 ± 0.1
Field	-	121	101	$-4.6^{+0.4}_{-0.5}$	$-0.48^{+0.08}_{-0.09}$	2.3 ± 0.2	1.31 ± 0.01	0.48 ± 0.03
Filament	-	136	106	$-4.4^{+0.3}_{-0.4}$	$-0.5^{+0.1}_{-0.2}$	1.9 ± 0.2	1.34 ± 0.01	$0.56^{+0.04}_{-0.03}$
Cluster	-	38	28	-3.4 ± 0.5	$0.0^{+0.1}_{-0.2}$	$1.9^{+0.4}_{-0.3}$	1.52 ± 0.03	$1.1^{+0.2}_{-0.1}$
$-1.5 \leq \log_{10}(SFR M_{\odot}\text{yr}^{-1}) < 0.4$	-	98	38	-1.4 ± 0.2	$-0.1^{+0.1}_{-0.3}$	$1.9^{+0.2}_{-0.3}$	1.47 ± 0.01	$0.92^{+0.08}_{-0.07}$
$0.4 \leq \log_{10}(SFR M_{\odot}\text{yr}^{-1}) < 0.8$	-	48	48	$-7.9^{+0.9}_{-0.7}$	$-0.19^{+0.06}_{-0.07}$	1.4 ± 0.2	1.32 ± 0.02	0.50 ± 0.04
$0.8 \leq \log_{10}(SFR M_{\odot}\text{yr}^{-1}) < 1.2$	-	48	48	$-6.9^{+0.4}_{-0.7}$	$-0.7^{+0.1}_{-0.2}$	2.4 ± 0.2	$1.29^{+0.01}_{-0.02}$	$0.44^{+0.03}_{-0.04}$
$1.2 \leq \log_{10}(SFR M_{\odot}\text{yr}^{-1}) < 3.0$	-	101	101	-10.3 ± 0.5	-0.8 ± 0.1	$2.6^{+0.2}_{-0.3}$	1.19 ± 0.01	0.22 ± 0.02
$-1.0 \leq \log_{10}(1 + \delta) < 0.1$	$10.0 \leq \log_{10}(M/M_{\odot}) < 10.5$	49	44	-9^{+1}_{-2}	$-0.6^{+0.2}_{-0.1}$	2.6 ± 0.4	$1.23^{+0.01}_{-0.02}$	$0.32^{+0.06}_{-0.05}$
$-1.0 \leq \log_{10}(1 + \delta) < 0.1$	$10.5 \leq \log_{10}(M/M_{\odot}) < 11.0$	63	55	$-3.7^{+0.4}_{-0.5}$	-0.5 ± 0.2	1.7 ± 0.2	$1.31^{+0.01}_{-0.02}$	0.46 ± 0.03
$-1.0 \leq \log_{10}(1 + \delta) < 0.1$	$11.0 \leq \log_{10}(M/M_{\odot}) < 12.0$	21	11	$-3.4^{+0.5}_{-0.4}$	$0.0^{+0.01}_{-0.04}$	$0.7^{+0.5}_{-0.7}$	$1.39^{+0.03}_{-0.02}$	$0.64^{+0.06}_{-0.07}$
$0.1 \leq \log_{10}(1 + \delta) < 0.6$	$10.0 \leq \log_{10}(M/M_{\odot}) < 10.5$	50	47	$-8.0^{+0.7}_{-0.9}$	$-0.4^{+0.1}_{-0.3}$	1.9 ± 0.3	1.23 ± 0.02	$0.30^{+0.05}_{-0.04}$
$0.1 \leq \log_{10}(1 + \delta) < 0.6$	$10.5 \leq \log_{10}(M/M_{\odot}) < 11.0$	57	48	-5.2 ± 0.4	$-0.4^{+0.1}_{-0.4}$	$1.7^{+0.4}_{-0.3}$	1.36 ± 0.02	$0.61^{+0.04}_{-0.05}$
$0.1 \leq \log_{10}(1 + \delta) < 0.6$	$11.0 \leq \log_{10}(M/M_{\odot}) < 12.0$	12	4	-2^{+1}_{-2}	$-0.2^{+0.2}_{-0.1}$	$1.8^{+0.3}_{-0.2}$	$1.54^{+0.05}_{-0.06}$	$1.2^{+0.7}_{-0.3}$
$0.6 \leq \log_{10}(1 + \delta) < 2.0$	$10.0 \leq \log_{10}(M/M_{\odot}) < 10.5$	8	4	-0^{+1}_{-4}	$-0.6^{+0.6}_{-0.1}$	2^{+1}_{-2}	1.47 ± 0.05	1.1 ± 0.2
$0.6 \leq \log_{10}(1 + \delta) < 2.0$	$10.5 \leq \log_{10}(M/M_{\odot}) < 11.0$	28	18	$-4.0^{+0.5}_{-0.6}$	N/A	$1.7^{+0.4}_{-0.3}$	1.48 ± 0.02	0.9 ± 0.1
$0.6 \leq \log_{10}(1 + \delta) < 2.0$	$11.0 \leq \log_{10}(M/M_{\odot}) < 12.0$	7	4	-2^{+1}_{-2}	$0.0^{+0.1}_{-0.4}$	1 ± 1	1.8 ± 0.1	5^{+3}_{-2}
$\log_{10}(sSFR) < -11$	$\log_{10}(1 + \delta) < 0.1$	25	0	$-2.4^{+0.4}_{-0.5}$	$0.0^{+0.1}_{-0.5}$	2 ± 1	1.34 ± 0.03	$0.54^{+0.09}_{-0.07}$
$\log_{10}(sSFR) < -11$	$\log_{10}(1 + \delta) > 0.4$	29	0	$-0.6^{+0.3}_{-0.2}$	N/A	$2.5^{+0.4}_{-0.3}$	$1.60^{+0.03}_{-0.02}$	$2.2^{+0.1}_{-0.4}$
$\log_{10}(sSFR) > -11$	$\log_{10}(1 + \delta) < 0.1$	234	234	-5.5 ± 0.4	-0.3 ± 0.1	1.6 ± 0.2	1.274 ± 0.010	0.39 ± 0.02
$\log_{10}(sSFR) > -11$	$\log_{10}(1 + \delta) > 0.4$	80	80	$-6.3^{+0.7}_{-0.9}$	-0.6 ± 0.2	2.4 ± 0.3	1.31 ± 0.02	$0.47^{+0.05}_{-0.04}$
Field	$10.0 \leq \log_{10}(M/M_{\odot}) < 10.5$	50	45	-6^{+1}_{-2}	-0.9 ± 0.2	3.2 ± 0.3	$1.31^{+0.01}_{-0.03}$	0.6 ± 0.1
Field	$10.5 \leq \log_{10}(M/M_{\odot}) < 11.0$	55	50	-3.9 ± 0.4	-0.1 ± 0.1	2.0 ± 0.3	1.30 ± 0.01	0.45 ± 0.03
Field	$11.0 \leq \log_{10}(M/M_{\odot}) < 12.0$	16	6	$-3.7^{+0.4}_{-0.3}$	N/A	N/A	1.35 ± 0.03	$0.55^{+0.08}_{-0.07}$
Filament	$10.0 \leq \log_{10}(M/M_{\odot}) < 10.5$	51	46	-8 ± 1	$-0.5^{+0.1}_{-0.2}$	$1.8^{+0.4}_{-0.3}$	1.20 ± 0.02	0.24 ± 0.04
Filament	$10.5 \leq \log_{10}(M/M_{\odot}) < 11.0$	66	50	-3.8 ± 0.3	-0.5 ± 0.2	2.0 ± 0.3	$1.39^{+0.01}_{-0.02}$	0.68 ± 0.03
Filament	$11.0 \leq \log_{10}(M/M_{\odot}) < 12.0$	19	10	$-1.6^{+0.3}_{-0.5}$	$-0.15^{+0.05}_{-0.09}$	1.7 ± 0.4	1.60 ± 0.03	$2.0^{+0.2}_{-0.5}$
Cluster	$10.0 \leq \log_{10}(M/M_{\odot}) < 10.5$	6	4	-4^{+1}_{-3}	$-0.3^{+0.3}_{-0.2}$	4^{+6}_{-1}	1.5 ± 0.1	1 ± 1
Cluster	$10.5 \leq \log_{10}(M/M_{\odot}) < 11.0$	27	21	$-3.0^{+0.6}_{-0.5}$	$-0.1^{+0.1}_{-0.5}$	2.0 ± 0.6	1.46 ± 0.03	$0.9^{+0.2}_{-0.1}$
Cluster	$11.0 \leq \log_{10}(M/M_{\odot}) < 12.0$	5	3	-1 ± 1	N/A	2^{+6}_{-1}	$2.0^{+0.1}_{-0.3}$	9^{+1}_{-6}